Interface-induced enhanced magnetocaloric effect in an epitaxial $CoFe_2O_4/La_{0.7}Sr_{0.3}MnO_3$ heterostructure

Abhisikta Barman,[1] Subhashree Chatterjee,[1] Jayjit Kr. Dey,[1] Anuja Datta,[2] and Devajyoti Mukherjee[1,*]

[1]*School of Physical Sciences, Indian Association for the Cultivation of Science, 2A & 2B Raja S. C. Mullick Road, Kolkata 700032, India*

[2]*School of Applied and Interdisciplinary Sciences, Indian Association for the Cultivation of Science, 2A & 2B Raja S. C. Mullick Road, Kolkata 700032, India*

(Received 16 July 2019; accepted 29 July 2020; published 24 August 2020)

An enhanced magnetocaloric effect is being reported in a strain-engineered ferrite-manganite heterostructure driven by a low temperature magnetostructural phase transition. An ultrathin (∼20 nm) epitaxial $CoFe_2O_4/La_{0.7}Sr_{0.3}MnO_3$ (CFO/LSMO) heterostructure was grown on single crystal MgO (100) substrate using pulsed laser deposition. Both temperature dependent x-ray diffraction and magnetization measurements revealed a broad second-order-type magnetostructural phase transition near around 80 K in the CFO/LSMO heterostructure. From detailed theoretical analysis of the experimental data it is confirmed that the phase transition around 80 K is second-order in nature, unlike the first-order transition observed in the bulk CFO materials. Thermodynamic analyses of magnetization reveal extremely broad isothermal entropy changes $\Delta S(T)$ about a wide range of temperatures ($40 < T < 160$ K) resulting in enhanced relative cooling powers which are higher than those reported so far on most magnetocaloric materials. We propose that an interfacial strain-induced magnetostructural coupling of the CFO layer with the underlying LSMO layer gives rise to these hitherto unobserved enhanced magnetocaloric effects in the CFO/LSMO heterostructure system. The work provides fundamental insight into the low temperature phase transitions in ferrite-manganite thin films and adds on to the design of artificial heterostructures with novel and enhanced magnetocaloric properties.

DOI: 10.1103/PhysRevB.102.054433

I. INTRODUCTION

Ferroic phase transitions in magnetic materials are commonly investigated for understanding magnetocaloric (MC) effects, i.e., the presence of reversible thermal (or entropy) changes in response to applied magnetic fields [1,2]. Recently, research on MC materials have gathered momentum due to their energy-efficient and eco-friendly solid-state cooling applications [3–6]. In terms of prototype design and performance, MC refrigeration is considered by far the most advanced and leading technology for solid-state caloric cooling with the first room-temperature MC refrigerator model demonstrated as early as 1976 [7], followed by a few MC prototype designs focusing mainly on room temperature MC refrigeration [8,9].

Theoretically, the choice of an ideal MC material depends on the parameters that quantify MC effects, namely, the adiabatic temperature change ΔT and the isothermal entropy change ΔS (or isothermal heat Q). At a temperature T, ΔS of a magnetic material due to an applied magnetic field H may be generally obtained from the Maxwell relation $\left(\frac{\partial S}{\partial H}\right)_T = \left(\frac{\partial M}{\partial T}\right)_H$ using [6]

$$\Delta S = \int_{H_1}^{H_2} \left(\frac{\partial M(T,H)}{\partial T}\right)_H dH. \tag{1}$$

Equation (1) implies that the temperature dependence of magnetization is coupled with an entropy change on varying the magnetic field. This indirect method has been successfully used to predict the performance of the MC materials [2]. Another important parameter that measures how much heat can be transferred from the cold end to the hot end in a refrigeration cycle is the relative cooling power (RCP), defined as [1,2]

$$\mathrm{RCP} = \int_{T_1}^{T_2} |\Delta S| \delta T_{\mathrm{FWHM}}, \tag{2}$$

where δT_{FWHM} is the full width half maximum of the $\Delta S(T)$ curve. An efficient prototype MC material should exhibit large values of the δT_{FWHM} along with increased ΔS for a significant temperature difference between the hot and the cold ends of the operating refrigeration cycle [10,11]. Based on this theory, till date large MC effects have been reported near the first-order magnetostructural phase transitions [12] in rare-earth alloys such as Gd [7], $Gd_5Si_{4-x}Ge_x$ [13,14], $MnAs_{1-x}Sb_x$ [15], MnFeP(As, Ge) [16], $LaFe_{13-x}Si_x$ [17], RM_2 (where R = rare earth, M = Al, Co, Ni) [18–20] and perovskite-oxides such as $La_xSr_{1-x}MnO_3$, $DyMnO_3$ [21]; along with a few studies on rare-earth oxides such as Eu_3O_4 [22] and $Gd_3Al_5O_{12}$ [23]. These findings have fuelled a considerable urge to search for MC effects in materials near their ferroic phase transitions for potential magnetic refrigeration applications [1]. The MC materials efficiency, defined as $\eta = |Q/W|$ (where W is the electrical or mechanical work done to drive

*Corresponding author: sspdm@iacs.res.in

MC effects to produce heat Q) [24], is found to be more than ten times higher when MC materials are mechanically driven using permanent magnets which can produce around 2 T fields rather than when driven electrically using solenoids which can produce higher fields (∼2 to 5 T) [6]. Hence, it is crucial to search novel MC materials exhibiting large $\Delta S(T)$ while being driven by nominal fields (<2 T) that can be generated by permanent magnets.

MC materials can be classified into the order of phase transitions that they undergo either first- or second-order type phase transitions [25]. The first-order MC materials have the advantages of exhibiting large magnetic entropy change $\Delta S(T)$ due to the coupling of the structural and magnetic transitions. However, they characteristically suffer from thermal or magnetic hysteresis losses, which give low efficiencies of the magnetic refrigeration cycles [26]. In addition, first-order MC materials show entropy changes only around a narrow temperature range about the phase transition temperature (Curie temperature T_C) of the magnetic material, which drastically reduces the operation temperature range of the devices [27]. On the other hand, the second-order MC materials do not suffer from thermal hysteresis but their MC responses are usually smaller than those of most first-order materials operating within the same temperature range [27,28]. Therefore, a current goal of magnetocalorics is to combine the best from both types of materials: large $\Delta S(T)$ response with minimum hysteresis loss and giving large RCP values. MC materials in single phase or in composite systems that can overcome these limitations individually or collectively are therefore highly desirable for future prototype solid state cooling technology.

In this direction, artificially engineered magnetic heterostructures, in particular epitaxial thin film heterostructures, are desirable [29]. Due to the effective clamping of the thin film material to the underlying layer or substrate it can suppress any additional structural transition and may likely broaden $\Delta S(T)$ over a particular temperature window; potentially enhancing the RCP [30]. However, reduced dimensions in MC thin films and heterostructures often lead to the unwanted loss of long-range ferromagnetic order and large local magnetic disorder at the surfaces and interfaces [31–40], thereby significantly decreasing $\Delta S(T)$ and consequently low RCPs [37,38,41]. Structural manipulations at the nanoscale in thin films via interface effects, chemical doping, or strain engineering may influence the phase transition temperatures in MC thin films [31–33,42–45]. Furthermore, epitaxial thin film heterostructures comprising magnetic and ferroelectric materials can promisingly enhance MC effects due to the cross coupling of ferroic order parameters at the interfaces [46].

From the materials' perspective, inverse spinel cobalt ferrite, $CoFe_2O_4$ (CFO), is one of the technologically important members of the ferrite family for its applications in magnetic spin filtering, spintronics, magnetic recording, and multiferroic devices [47–49]. CFO has a high T_C of 793 K below which it exhibits long-range ferrimagnetic order with antiferromagnetic intersublattice exchange interactions. CFO also has a moderate saturation magnetization ($M_{sat} \approx 400\,\mathrm{emu/cm^3}$), high magnetocrystalline anisotropy constant ($K_1 \sim 2\times10^5\,\mathrm{J\,m^{-1}}$) and high coercivity ($H_c \approx 0.2\,\mathrm{T}$) [49]. Combined with these properties, the various temperature driven phase transitions (2–800 K) in CFO can make it a promising candidate for investigating MC effects. Notably, bulk CFO undergoes a first-order structural phase transition from cubic ($Fd3m$) to monoclinic (Cc) (i.e., almost tetragonal; $a \approx b < c$, $\alpha = 90.2°$, $\beta = \gamma = 90°$) phase at around 90 K [50–52] (Verwey transition) and is concomitant with drastic changes in the electrical, magnetic, and thermal properties around this Verwey transition temperature (T_V) [53–57]. Recently, MC effects have been reported near the T_V (≈120 K) [58,59] in unstrained polycrystalline Fe_3O_4 thin films [55,56] with narrow widths of the $\Delta S(T)$ curves around T_V, resulting in low RCP values [60]. To this end, strained epitaxial thin films of CFO (100) can possess high magnetocrystalline anisotropy making them interesting candidates to investigate MC effects around the T_V [61,62].

In this work we report on the observation of an enhanced MC effect near the Verwey transition from an ultrathin (∼20 nm) CFO film, epitaxially grown on an underlying layer of the half-metallic ferromagnet $La_{0.7}Sr_{0.3}MnO_3$ (LSMO) on single crystal MgO (100) substrate using pulsed laser deposition (PLD) technique. The underlying LSMO layer was designed in the structure to enhance the saturation magnetization of the heterostructure. Using in-depth temperature dependent x-ray analyses, we show that the structural transformation in CFO thin films occur below the Verwey transition. The manifestation of Verwey transition in epitaxial CFO/LSMO thin films is hitherto unobserved in these systems. Our magnetic measurements revealed an enhanced magnetization in the epitaxial CFO/LSMO thin film as compared to their single layers grown with the same method. Thermodynamic analyses of the magnetization showed a reasonable isothermal magnetic entropy change ($|\Delta S| = 0.63\,\mathrm{J\,kg^{-1}K^{-1}}$) about a substantial range of temperature ($40 < T < 160\,\mathrm{K}$) in 1 T magnetic field. The extremely broad $\Delta S(T)$ curves resulted in enhanced relative cooling powers ($\mathrm{RCP_{max}} = 73\,\mathrm{J\,kg^{-1}}$ at 1 T) which is unprecedented in magnetic systems reported so far. The enhanced MC effect in the sample is concluded to be due to a strain induced magnetostructural coupling in the epitaxial heterostructure near the Verwey transition.

II. EXPERIMENT

CFO/LSMO heterostructures were grown on single-crystal MgO (100) substrates using a commercial pulsed laser deposition (PLD; Neocera Pioneer 120 Advanced) system. Briefly, high-purity ceramic targets of $La_{0.7}Sr_{0.3}MnO_3$ and $CoFe_2O_4$ were prepared from commercially bought powders from Alfa Aesar with high purity (99.99%) via pressing and sintering at 1200 °C. The prepared targets were characterized for phase purity and composition. The LSMO and CFO targets were then sequentially ablated using a KrF excimer laser (Lambda Physik, $\lambda = 248\,\mathrm{nm}$, frequency $= 10\,\mathrm{Hz}$, fluence $= 30\,\mathrm{kJ\,m^{-2}}$) inside a deposition chamber equipped with a multitarget carousel that allowed for the *in situ* deposition of multilayers with clean interfaces. A distance of 5 cm was maintained between the substrate and the targets during the depositions. Prior to growing the LSMO layer, the MgO substrate was annealed inside the PLD chamber at 800 °C under a background oxygen pressure (pO_2) of 500 mTorr for 2 h. In the optimized synthesis process, an initial layer of LSMO was deposited onto an MgO substrate at 800 °C

under a background pO_2 of 10 mTorr, followed by the CFO layer at 450 °C with pO_2 of 10 mTorr. After deposition, the PLD chamber was flooded with pure oxygen (500 mTorr) and the samples were gradually cooled down to room temperature (∼2 h). For comparison, LSMO and CFO single-layer films were also grown on MgO (100) substrates under the same conditions. The thicknesses of the LSMO and CFO were kept constant at ∼60 and ∼20 nm, respectively. While several samples were deposited to optimize the growth conditions, here we only present the results from the optimized CFO/LSMO sample.

The crystallinity and crystallographic orientations in the heterostructures were characterized by x-ray diffraction (XRD) with a Rigaku Smart Lab 9 kW XG diffractometer equipped with a 5-axis goniometer and temperature variable thin film sample stage using collimated parallel beam Cu $K\alpha$ radiation ($\lambda = 1.5406$ Å). Thermal conductive grease was used to fix the samples on the thin film temperature stage of the XRD and care was taken to avoid sample misalignment. Raman spectra were measured at room temperature using a laser Raman spectrophotometer (JY Horiba-T6400 equipped with a Synopse CCD camera) using a Nd:YAG laser (532 nm) over the range of 150−900 cm^{-1}. The Raman spectra reported here have been deconvoluted into individual Lorentzian peaks for accurate peak positioning. X-ray photoelectron spectra (XPS) were measured using a commercial Omicron (model 1712-62-11) spectrometer. The data were collected at room temperature using a nonmonochromatic Al $K\alpha$ (1486.7 eV) x-ray source operating at 150 W (15 kV and 10 mA). The surface morphologies were observed using an atomic force microscope (AFM, Digital Instruments III). Interfacial microstructure in the CFO/LSMO heterostructure was analyzed using high-resolution transmission electron microscopy (HRTEM; FEI Tecnai F 20 S-Twin TEM). A sample for cross-sectional TEM analysis was prepared by surface milling a 5 μm×10 μm rectangular strip of 100 nm thickness using a focused ion beam (FIB; JOEL 4500 FIB/SEM) and Pt-welding it to a Cu TEM grid. A protective Pt layer as seen in Fig. 3(a) was used to preserve the features of the heterostructure during FIB milling for TEM sample preparation. Electrical conductivities of the thin film samples were measured using a four-point configuration with a Physical Property Measurement System (PPMS) (Quantum Design Inc. DynaCool 9T). For electrical measurements Pt top electrodes of 0.2 mm diameter were sputtered on the film surfaces using a shadow mask. Magnetic measurements were performed using a commercial superconducting quantum interference device (SQUID) magnetometer (Quantum Design, Inc.) in the temperature range from 2 to 320 K in magnetic field up to 5 T. Magnetization versus magnetic field $M(H)$ loops are reported after the subtraction of the diamagnetic contribution from the MgO substrates.

III. RESULTS AND DISCUSSION

A. Crystallinity, stoichiometry, and surface morphology

Bulk CFO (fcc, $a = 8.39$ Å) has a very small lattice mismatch (∼0.35%) with the underlying MgO (cubic, $2xa = 2\times4.21$ Å $= 8.42$ Å) (100) substrate in the CFO/MgO thin film while it has a significant lattice mismatch (∼7%–8%) with the underlying LSMO (pseudocubic, $2xa = 2\times3.87$ Å $= 7.74$ Å) layer in the CFO/LSMO/MgO heterostructure [61,63]. The single crystalline nature of the CFO (∼20 nm) and LSMO (∼60 nm) phases in CFO/LSMO/MgO heterostructure and CFO/MgO thin film are evidenced from the XRD θ-2θ patterns shown in Fig. 1(a). The patterns show only the (400) peak of fcc CFO phase (JCPDS 00-022-1086) and the (200) peak of pseudocubic perovskite LSMO phase (JCPDS 01-089-4461) alongside the (200) peak of the MgO substrate, confirming the unidirectional epitaxial growth with no traces of impurity peaks within the resolution limits of the XRD. Due to the close proximity of the CFO (400) and the MgO (200) peaks, a close-up view of CFO/LSMO is shown in inset (I) of Fig. 1(a), where the dotted line marks the position of the CFO (400) peak from the CFO powder XRD data [61,64]. As compared to the unstrained cubic bulk CFO with a lattice parameter of $a_o = 8.390$ Å, the occurrence of the CFO (400) peak at lower 2θ values in CFO/LSMO heterostructure implies elongation of the out-of-plane lattice parameter (a_{per}) of the CFO unit cell [61]. Inset (II) in Fig. 1(a) shows the asymmetric XRD 2θ-ω scan (or detector scan) about the CFO (311) plane in the heterostructure. The occurrence of the (311) peak at higher 2θ values as compared to the bulk position (marked by a dotted line) suggests a contraction of the in-plane lattice parameter (a_{par}) of the CFO unit cell in the film. This is easily understood since the CFO unit cell may experience an in-plane compressive strain (i.e., out-of-plane tensile strain) in order to match the slightly smaller lattice parameter of the underlying LSMO layer [49]. As listed in Table I, the calculated values for $a_{per} = 8.465(6)$ Å and $a_{par} = 8.354(5)$ Å gives an out-of-plane tensile strain $\varepsilon_{per} = (a_{per} - a_o)/a_o \approx 0.8\%$ and correspondingly an in-plane compressive strain $\varepsilon_{par} = (a_{par} - a_o)/a_o \approx -0.4\%$ in the CFO layer in CFO/LSMO heterostructure. This results in an out-of-plane tetragonal distortion (i.e., $a_{per}/a_{par} - 1$) of ∼1.2% in the CFO unit cell in CFO/LSMO as compared to the bulk cubic CFO unit cell. In contrast for the CFO thin film on MgO substrate, the calculated values for $a_{per} = 8.388(6)$ Å and $a_{par} = 8.401(2)$ Å gives a very small out-of-plane compressive strain $\varepsilon_{per} = (a_{per} - a_o)/a_o \approx 0.01\%$ and correspondingly a slight in-plane tensile strain $\varepsilon_{par} = (a_{par} - a_o)/a_o \approx 0.1\%$ in the CFO layer. This results in a much smaller tetragonal distortion (i.e. $a_{per}/a_{par} - 1$) of ∼0.1% in the CFO unit cell in CFO thin film on MgO as compared to that in the CFO/LSMO heterostructure of 1.2% [65]. From the XRD measurements it is clear that the tetragonal distortion of CFO when grown on LSMO is 1.2% in CFO/LSMO/MgO heterostructure while when directly grown on MgO is 0.1% in the CFO/MgO thin film (due to the close lattice match of CFO with MgO). Since CFO is a highly magnetostrictive material, the larger tetragonal distortion of the CFO layer in CFO/LSMO/MgO as compared to CFO/MgO could drastically affect its magnetization and the MC properties [66]. The epitaxial growth of the individual layers of CFO and LSMO on the MgO substrate was further confirmed from XRD φ (phi or azimuthal) scans [49] performed about the MgO (111), LSMO (111), and CFO (222) crystallographic planes, respectively, as shown in Fig. 1(b). These crystallographic planes of the CFO, LSMO, and MgO phases were specifically chosen for the XRD φ

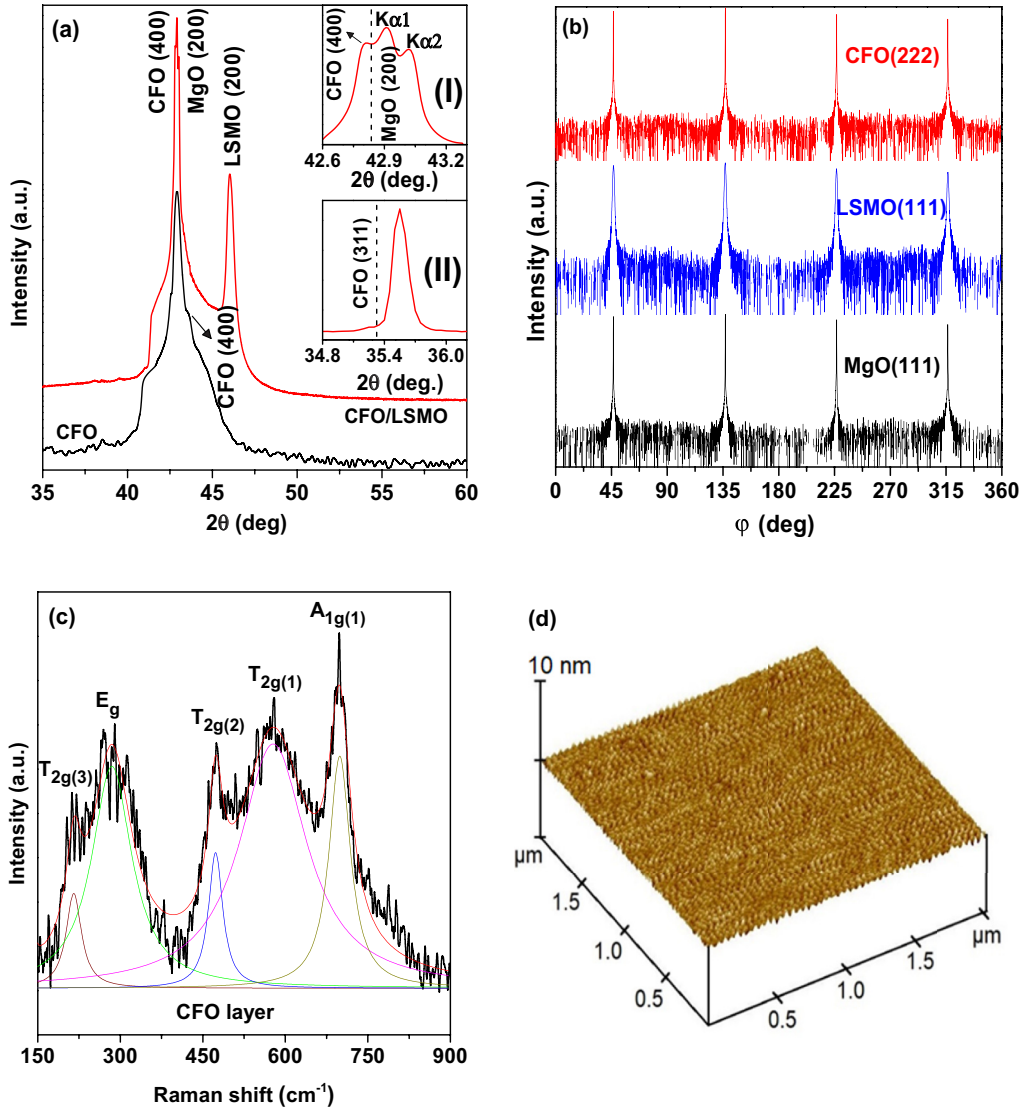

FIG. 1. (a) XRD θ-2θ patterns for the CFO/MgO thin film and the CFO/LSMO/MgO heterostructure. Inset (I) to (a) shows a close-up view of the CFO (400) and the MgO (200) peaks in the CFO/LSMO/MgO heterostructure. Inset (II) to (a) shows an asymmetric XRD 2θ-ω scan performed about the CFO (311) crystallographic plane for the CFO/LSMO/MgO heterostructure. (b) Representative XRD azimuthal (φ) scans performed about the CFO (222), LSMO (111), and MgO (111) crystallographic planes for the CFO/LSMO/MgO heterostructure. (c) Room temperature Raman spectrum of the CFO layer captured from the CFO/LSMO/MgO heterostructure. (d) Representative AFM image of the top CFO surface captured from the CFO/LSMO/MgO heterostructure. The z height on the AFM image is 10 nm.

scans so that there is no contribution from underlying phases in the CFO/LSMO heterostructure. The repeated occurrence of sharp peaks at regular intervals of 90° confirms the fourfold symmetry of the individual layers and cube-on-cube epitaxial growth of the heterostructure. Rocking scans (Fig. S1 in the Supplemental Material [67]) performed about the CFO (400) plane showed extremely narrow width (FWHM = 0.1°) which further confirmed the in-plane orientation of the CFO layer in the CFO/LSMO heterostructured epitaxial film.

Raman spectroscopy was used to investigate the short-range site ordering of the cations in the heterostructure. Figure 1(c) shows the characteristic Raman spectrum of the

TABLE I. Structural and strain parameters of the CFO layer in CFO/MgO and CFO/LSMO/MgO heterostructures determined from XRD measurements: out-of-plane lattice parameter (a_{per}), in-plane lattice parameter (a_{par}), out-of-plane strain (ε_{per}), in-plane strain (ε_{par}), and in-plane stress (σ_{par}).

Sample	Lattice mismatch (%)	a_{per}(Å)	a_{par}(Å)	ε_{per}(%)	ε_{par}(%)	σ_{par}(Nm^{-2})
CFO/MgO	0.35	8.388(6)	8.401(2)	0.01	0.1	1.5×10^{8}
CFO/LSMO/MgO	7.39	8.465(6)	8.354(5)	0.8	−0.4	-6×10^{8}

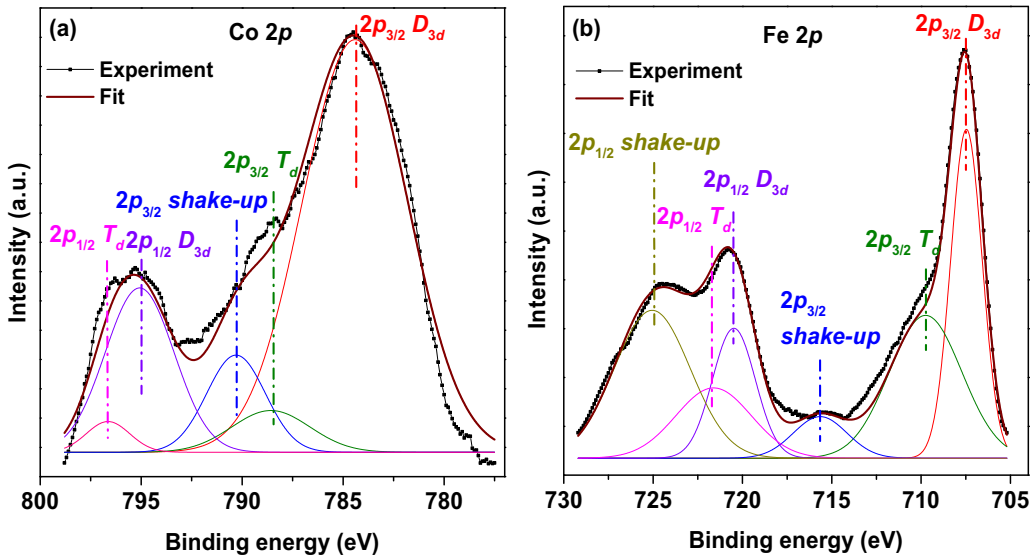

FIG. 2. X-ray photoelectron spectra of (a) Co $2p$ and (b) Fe $2p$ core levels as measured from the top CFO layer for the CFO/LSMO heterostructure. Each sublevel ($2p_{3/2}$ and $2p_{1/2}$) splits into a tetrahedral component (T_d), an octahedral one (D_{3d}), and a shake-up satellite.

CFO layer in the heterostructure. As typically observed, five distinct peaks at ∼197, ∼312, ∼471, ∼579, and ∼694 cm^{-1} corresponding to the five Raman active modes of vibrations ($A_{1g} + E_g + 3T_{2g}$) confirm the inverse spinel structure and the preservation of the cation distribution in the CFO layer [68]. Figure 1(d) shows a representative AFM image of the top CFO layer in CFO/LSMO which exhibits smooth particulate-free surface morphology with extremely low roughness (R_{rms} ∼ 1 nm at z height of 10 nm) and uniform grain sizes, corroborating high quality of the prepared sample. Close observation of the AFM image reveals a subnanometer step-terrace structure on the surface of the CFO film that authenticates its layer-by-layer growth morphology, typical of PLD grown epitaxial layers.

X-ray photoelectron spectra were collected *ex situ* from the CFO/LSMO heterostructure to determine the inversion parameter of CFO [69,70]. Figures 2(a) and 2(b) show the experimental Co $2p$ and Fe $2p$ core-level photoemission spectra obtained from the CFO top layer in CFO/LSMO heterostructure, respectively. Following the approach described by Santis *et al.* [69] and Aghavnian *et al.* [70], the whole experimental spectrum was fitted but only the $2p_{3/2}$ component was taken into account since its higher intensity gave greater precision. In the inverse-spinel structure of CFO, the Co ions are divalent, and a splitting is observed for atoms on octahedral (B, D_{3d} symmetry) and tetrahedral (A, T_d symmetry) sites. Each sublevel further exhibits a shake-up satellite peak due to the excitation of a $3d$ electron by the core-level photoelectron. Considering this, the Co $2p$ level in Fig. 2(a) was fitted with three doublets, after subtraction of a Shirley-type background. The inversion parameter, i.e., the fraction of Co ions on octahedral sites was calculated from the areas of the Co $2p_{3/2}-D_{3d}$ and Co $2p_{3/2}-T_d$ peaks in Fig. 2(a). The value of the inversion parameter was obtained to be 0.94, which is close to the theoretical value of 1 in bulk CFO. Since the Fe ion is trivalent in CFO, the equivalent analysis of the Fe $2p_{3/2}$ doublet shown in Fig. 2(b) provided an estimation that 50% of Fe ions are located on the tetrahedral sites. Since the binding energies of the elements depend on their valence states and on the local structural environment, the XPS analyses confirmed the correct composition and crystal structure of CFO in CFO/LSMO. The valence states of the

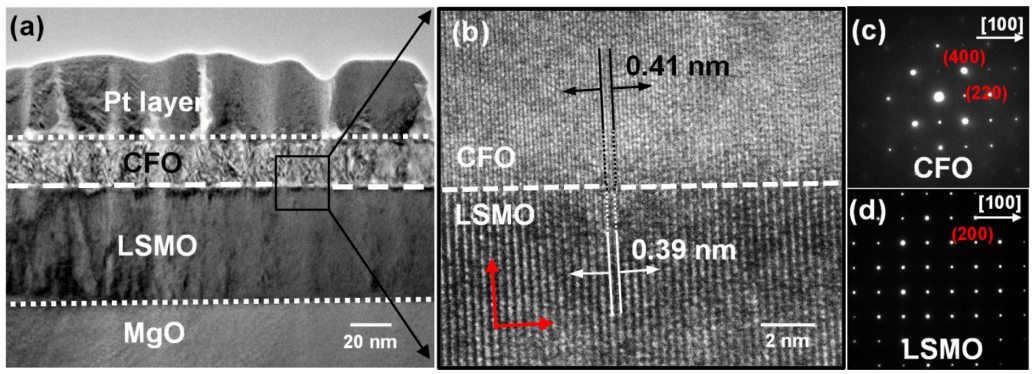

FIG. 3. (a) Cross-sectional TEM image of CFO/LSMO/MgO heterostructure. (b) HRTEM image of the CFO-LSMO interface captured from the region marked with black box in (a). (c) and (d) SAED patterns captured near the CFO and LSMO layers of CFO/LSMO/MgO heterostructure, respectively. The direction of the (100) plane is marked with a white arrow in (c) and (d).

various elements of the LSMO layer such as La, Sr, and Mn were determined from the XPS spectra of the individual elements as shown in Fig. S2 in the Supplemental Material [67], which was then used to infer the chemical stoichiometry of the LSMO layer in the CFO/LSMO heterostructure. In all cases, the correct composition of CFO and LSMO were obtained within the accuracy limits of the measurements [62], validating the optimized growth conditions used to deposit the sample.

B. Interfaces

A cross-sectional microstructure of the CFO/LSMO thin film revealed sharp and flat interfaces with uniform thicknesses of the individual layers, as illustrated in the representative TEM image in Fig. 3(a). The HRTEM image of the CFO/LSMO interface in Fig. 3(b) [captured from a region marked with a black box in Fig. 3(a)] shows atomically sharp and flat phase boundaries with continuous lattice fringes from the bottom LSMO layer to the top CFO layer. The red arrow shows the directions of the (001) (in-plane horizontal arrow) and (100) (out-of-plane vertical arrow) planes. The image clearly demonstrates the single crystalline nature and the cube-on-cube epitaxial growth morphology of the heterostructure. Similar HRTEM images captured at different locations along the CFO-LSMO interface showed no evidence of any structural defects such as lattice misfits or twin planes. The measured d-spacing values for CFO ($d = 0.41$ nm) and LSMO ($d = 0.39$ nm) in Fig. 3(b) are consistent with those obtained from the XRD analyses. The microcrystallinity in the sample was determined from the selected area diffraction (SAED) patterns captured at different locations along the interfaces and the individual layers. The linear dotted single-crystalline SAED pattern shown in Figs. 3(c) and 3(d) captured from the CFO and the LSMO layers, respectively, clearly showed the face centered cubic and pseudocubic crystal structures of the layers. From the TEM analyses, it is concluded that the CFO layer and the LSMO layer have almost identical lattice parameters near the interface in the CFO/LSMO heterostructure, suggesting a highly strained state in the CFO layer.

C. Structural phase transition

Figure 4(a) shows the temperature dependent XRD θ-2θ patterns about the CFO (400) and MgO (200) peaks for CFO/LSMO heterostructure as measured from 300 down to 60 K at regular intervals of 5 K (as shown in the scale bar) while cooling the sample. The XRD patterns in Fig. 4(a) have been purposefully shifted from right (300 K) to left (60 K) for visual clarity. The MgO (200) peaks are deconvoluted into two peaks for contributions from Cu $K_{\alpha 1}$ and $K_{\alpha 2}$ lines. The Cu (111) peak in each XRD pattern comes from the XRD sample holder which was chosen as a reference peak in the analyses. It is clearly observed from the XRD patterns in Fig. 4(a) that there is no change in the peak profiles or intensities of the bulk Cu (111) peaks or the MgO (200) substrate peaks, but a distinct change in the peak profile and intensity is observed in the CFO (400) peak as detailed in the close-up view in the inset to Fig. 4(a). Since the in-plane lattice parameter (a_{par}) of CFO could be strongly affected by the lattice mismatch of the underlying LSMO layer in CFO/LSMO, we plot the in-plane lattice parameters for the CFO unit cell in the temperature range of 300 to 60 K in Fig. 4(b) for predicting the structural phase transition in CFO/LSMO heterostructure [71]. Note that the error bars in Fig. 4(b) are calculated from the full width half maxima of the CFO (400) peaks shown in Fig. 4(a). The room temperature in-plane lattice parameter of CFO matches with that observed earlier in Fig. 1(a) for CFO/LSMO. From Fig. 4 it is observed that the in-plane lattice parameter first gradually decreases as the temperature decreases from 300 to 80 K due to the thermal contraction of the CFO unit cell with lowering the temperature. At around 79 K there is a sudden sharp increase in the lattice parameter which could indicate a possible structural phase transition in the CFO layer. In order to confirm this, we also measured temperature dependent XRD patterns from 60 to 200 K while heating the sample as shown in the XRD patterns in Fig. S3(a) in the Supplemental Material [67]. We observe a similar anomalous jump in the in-plane lattice parameter at around 80 K in the lattice parameter versus temperature plot as shown in Fig. S3(b) in the Supplemental Material [67]. From the temperature dependent XRD analyses, we can attribute this sharp change in lattice parameter at 79 K (cooling cycle) and 80 K (heating cycle) to the structural Verwey transition in the CFO layer in CFO/LSMO heterostructure. From Fig. 4(b) the Verwey transition temperature (T_V) is assigned to be around 79 K in CFO/LSMO heterostructure. Since there is almost no thermal hysteresis in the T_V in the heating and cooling cycles shown in Fig. S3(b) [67], it could indicate that the structural transition at T_V in CFO/LSMO is second-order in nature. Literature reports show that in unstrained bulk CFO the structural transition from its cubic (Fd-$3m$) phase to the predicted monoclinic ($P2/c$) phase (almost tetragonal structure) with ($a \approx b < c$, $\alpha = 90.2^\circ$, $\beta = \gamma = 90^\circ$) [50–52]. For $T < T_V$ ($<$79 K), the elongation of the in-plane lattice parameter in the monoclinic phase (almost tetragonal with $a \approx b < c$, $\alpha = 90.2^\circ$, $\beta = \gamma = 90^\circ$) as compared to the cubic phase is consistent with the existing theoretical models on the Verwey transition in ferrites since the monoclinic phase (almost tetragonal with $a \approx b < c$, $\alpha = 90.2^\circ$, $\beta = \gamma = 90^\circ$) of CFO unit cell is anisotropic with slightly larger c-axis lattice parameter [here in-plane lattice parameter in Fig. 4(b)] as compared to the isotropic cubic phase [59,72]. The temperature dependent XRD analyses also suggests that the c axis for the monoclinic phase ($a \approx b < c$, $\alpha = 90.2^\circ$, $\beta = \gamma = 90^\circ$) at $T < T_V$ could be along the in-plane direction. Due to the in-plane compressive strain we already show that there is an out-of-plane tetragonal distortion in the CFO unit cell in CFO/LSMO at room temperature with the c axis in the out-of-plane direction (see Table I). As temperature decreases below T_V, there could be a possible reorientation of the c axis from out-of-plane direction in the tetragonal phase ($a \approx b > c$, $\alpha = \beta = \gamma = 90^\circ$) to the in-plane direction in the monoclinic phase (i.e.. almost tetragonal with $a \approx b < c$, $\alpha = 90.2^\circ$, $\beta = \gamma = 90^\circ$) which consequently lowers the T_V to 79 K as compared to the observed 90 K in bulk unstrained samples [58,59]. It is also revealed from Fig. 4(b) that for $T < T_V$, the in-plane lattice parameter again decreases as temperature is decreased from 79 to 60 K. The mean linear coefficient of thermal expansion (α) calculated from the slopes of the linear fits of

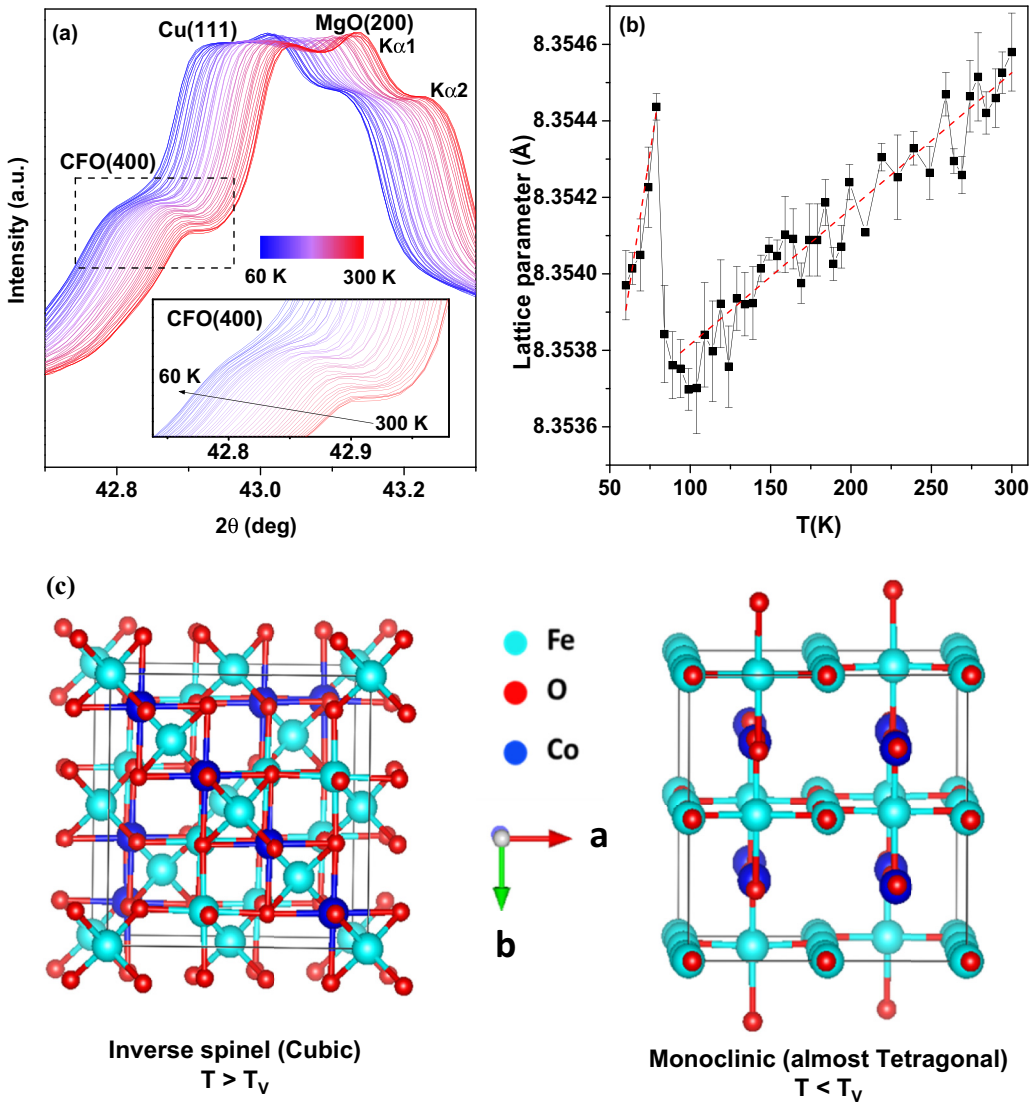

FIG. 4. (a) Temperature dependent XRD θ-2θ patterns from 300 to 60 K with regular intervals of 5 K (shown in scale bar) showing the detailed CFO (400) and MgO (200) peaks for CFO/LSMO/MgO heterostructure. The Cu (111) peak from XRD sample holder was chosen as a reference peak in the analysis. Inset to (a) shows the close-up view of the temperature evolution of the CFO (400) peak. (b) In-plane lattice parameters for the CFO unit cell at different temperatures calculated from the XRD patterns in (a). (c) Simulated CFO unit cells in VESTA software using XRD data in (a) showing the structures of inverse spinel phase at 100 K (left image) ($T > T_V$) and monoclinic phase at 79 K (right image) ($T < T_V$).

the data in Fig. 4(b) (red dotted lines as the eye guide) in the range $T > T_V$ is $\alpha_{(T>T_V)} = 0.43\times10^{-6}\,K^{-1}$ and $T < T_V$ is $\alpha_{(T<T_V)} = 3.25\times10^{-6}K^{-1}$, respectively, which is close to the values for bulk ferrites [73]. Figure 4(c) shows the simulated crystal structures of CFO unit cells with the inverse spinel phase at 100 K ($T > T_V$) (left image) ($a = b = c = 8.35$ Å, $\alpha = \beta = \gamma = 90^\circ$) and monoclinic phase at 75 K $T < T_V$ (right image) ($a = 8.34$, $b = 8.24$, $c = 8.46$ Å, $\alpha = 90.2^\circ$, $\beta = \gamma = 90^\circ$) using the temperature dependent XRD data in Fig. 4(a) and are consistent with previous results on bulk ferrite systems [59]. Details of the input parameters in the simulations are provided in Sec. S1 in the Supplemental Material [67]. It is noted that for simplicity the inversion parameter for CFO in the simulation has been considered to be the ideal value of 1 since from XPS analyses the inversion parameter was calculated to be 0.94 which is close to unity. Observation of the Verwey structural phase transition has been rarely evidenced since one of the major challenges in the low temperature structural refinement of the ferrite crystals from the cubic ($Fd3m$) ($a = b = c = 8.39$ Å, $\alpha = \beta = \gamma = 90^\circ$) to the monoclinic ($P2/c$) ($a \approx b < c, \alpha = 90.2^\circ, \beta = \gamma = 90^\circ$) phase is due to the extremely small degree of distortion in the CFO unit cell above and below T_V along with the presence of strong twinning in the lattice. Since the magnetic easy axis of the monoclinic structure (almost tetragonal; $a \approx b < c$, $\alpha = 90.2^\circ$, $\beta = \gamma = 90^\circ$) nearly coincides with one of the three original cubic (100) directions, it is difficult to resolve the structural change using XRD [72]. Hence observation of Verwey transition as understood from Fig. 4 might be imparted due to the oriented growth of the epitaxial heterostructured film with (100) orientation. Even though the degree of change in the lattice parameter around T_V is relatively small,

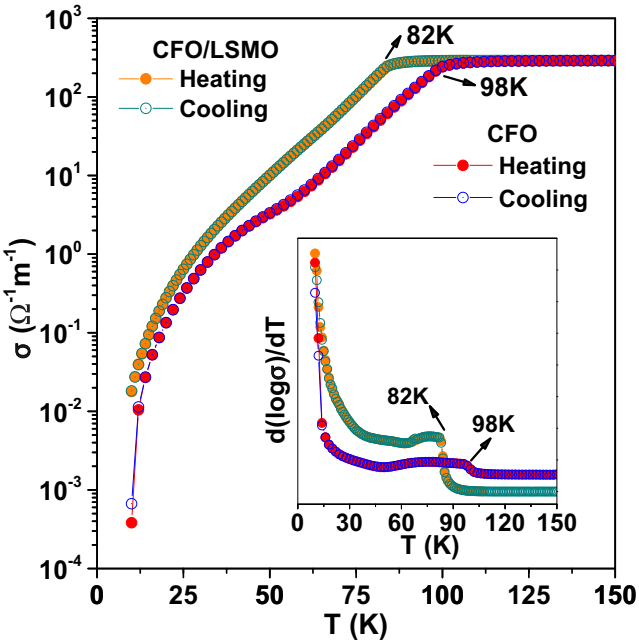

FIG. 5. Temperature dependent electrical conductivity $\sigma(T)$ of CFO thin film and CFO/LSMO heterostructure grown on MgO (100) substrate. Inset (I) to (a) shows $d(\log\sigma)/dT$ of CFO thin film and CFO/LSMO heterostructure. The open and closed symbols indicate the cooling and heating cycles, respectively.

it might be indicative of second-order transition phenomenon in our ferrite system.

D. Electrical properties

Figure 5 shows the temperature dependence of the electrical conductivity $\sigma(T)$ (in log scale) of the CFO layers as measured from the CFO thin film and CFO/LSMO heterostructure in the temperature range of 2–150 K in both heating and cooling cycles. The room temperature values for $\sigma(T)$ for both samples were almost the same at 300 $\Omega^{-1}\mathrm{m}^{-1}$ indicating the similar single crystalline quality of the samples. From Fig. 5 it is observed that the values for the $\sigma(T)$ for the CFO and CFO/LSMO samples match in the temperature range 100 to 150 K but the conductivity $\sigma(T)$ abruptly decreases by more than two orders in magnitude starting at 98 K for CFO thin film and at 82 K for CFO/LSMO heterostructure. The drop in the electrical conductivity at low temperatures as shown in Fig. 5 is attributed to the characteristic Verwey transition in these ferrite thin films [53,55,58]. The Verwey transition temperatures (T_V) for the CFO thin film and CFO/LSMO heterostructure as estimated from the peak positions of the $d(\log\sigma)/dT$ curves (shown in the inset to Fig. 5) were found to be around 98 K and 82 K, respectively. The origin of this metal-to-insulator transition is still under discussion, but it is interpreted that there occurs a charge order-disorder transition in the crystal structure in which the valence electrons order themselves over the octahedral sites (B sites) to form a Co^{2+} and Fe^{3+} superstructure in the insulating phase [53,54]. From Fig. 5 it is further observed that the $\sigma(T)$ values match with each other for both heating and cooling cycles for both samples indicating no thermal hysteresis in electrical conductivity around T_V. The absence of thermal hysteresis in $\sigma(T)$ near T_V provides evidence that the structural transition from cubic to monoclinic (nearly tetragonal, $a \approx b < c, \alpha = 90.2^\circ$, $\beta = \gamma = 90^\circ$) below T_V in CFO/LSMO thin films could be second-order in nature as opposed to the first-order transition observed in bulk CFO [58]. The existence of charge-orbital ordering in the CFO and CFO/LSMO films and their reversible phase transition around T_V could potentially make them promising candidates for MC studies [58]. The Verwey transition seen in $\sigma(T)$ measurements in CFO/LSMO is also accompanied by a minute structural change from a high-temperature cubic phase to a low-temperature monoclinic (or almost tetragonal) phase in CFO as evidenced from the XRD analysis in Fig. 4. The T_V (=82 K) for CFO/LSMO as measured from the $\sigma(T)$ is almost the same with that ($T_V = 80$ K) calculated from the temperature dependent XRD analyses in Fig. 4. The difference in the T_V values for the CFO and CFO/LSMO samples as seen in Fig. 5 could be attributed to their different epitaxial strains (i.e., in-plane tensile strain in CFO of 0.1% and in-plane compressive strain in CFO/LSMO of 0.4%), as observed in the XRD analyses [55]. This is consistent with the previous report of different T_V values observed for epitaxial Fe_3O_4 films grown under tensile and compressive strains on various single crystal substrates [55]. Epitaxial Fe_3O_4 (fcc, $a = 8.39$ Å) thin film when grown under in-plane compressive strain on $MgAl_2O_4$ (cubic, $a = 8.085$ Å) (100) substrate with a lattice mismatch of 4% exhibited lower T_V (94 K) while the Fe_3O_4 film grown under in-plane tensile strain on MgO (cubic, $2xa = 2\times4.21$Å $= 8.42$ Å) (100) substrate with a lattice mismatch of 0.1% exhibited higher T_V (108 K); in a similar manner as the CFO and CFO/LSMO films grown under different strains in this work.

E. Magnetic and magnetocaloric properties

Further confirmation on the Verwey transition is obtained from the temperature dependence of magnetization $M(T)$ for the single-layer CFO thin film as shown in Fig. 6(a). The Verwey transition temperature as measured from the peak position in the dM/dT curve for CFO thin film [shown in Fig. 6(a)] indicates $T_V = 100$ K which is very close to the value of T_V (=98 K) as measured from the conductivity measurements in Fig. 5. The inset to Fig. 6(a) shows the in-plane room temperature M-H loop for the CFO thin film measured to a maximum field of 5 T. A saturation magnetization ($M_S = 443 \pm 13\,\mathrm{kA\,m^{-1}}$) which corresponds to $3.5\mu_B$ per Co site, and large coercive field ($H_c = 0.35$ T) consistent with earlier reports on epitaxial CFO films on MgO substrates [61], is observed from the figure. However, the high saturating field ($H_{sat} = 3$ T) and the large coercive field ($H_c = 0.35$ T) as observed in Fig. 6(a) for the CFO thin film do not make it conducive for MC applications. Nevertheless, in order to compare the magnetic and MC properties of the CFO thin film and the CFO/LSMO heterostructure, here we have calculated the isothermal entropy change from the field and temperature dependent magnetization for CFO thin film. Figure 6(b) shows the isothermal magnetization $M(H)$ curves for CFO thin film as measured for 5 T fields for various temperatures starting from 200 to 40 K. The temperature dependent isothermal entropy change $\Delta S(T)$ was calculated from the temperature

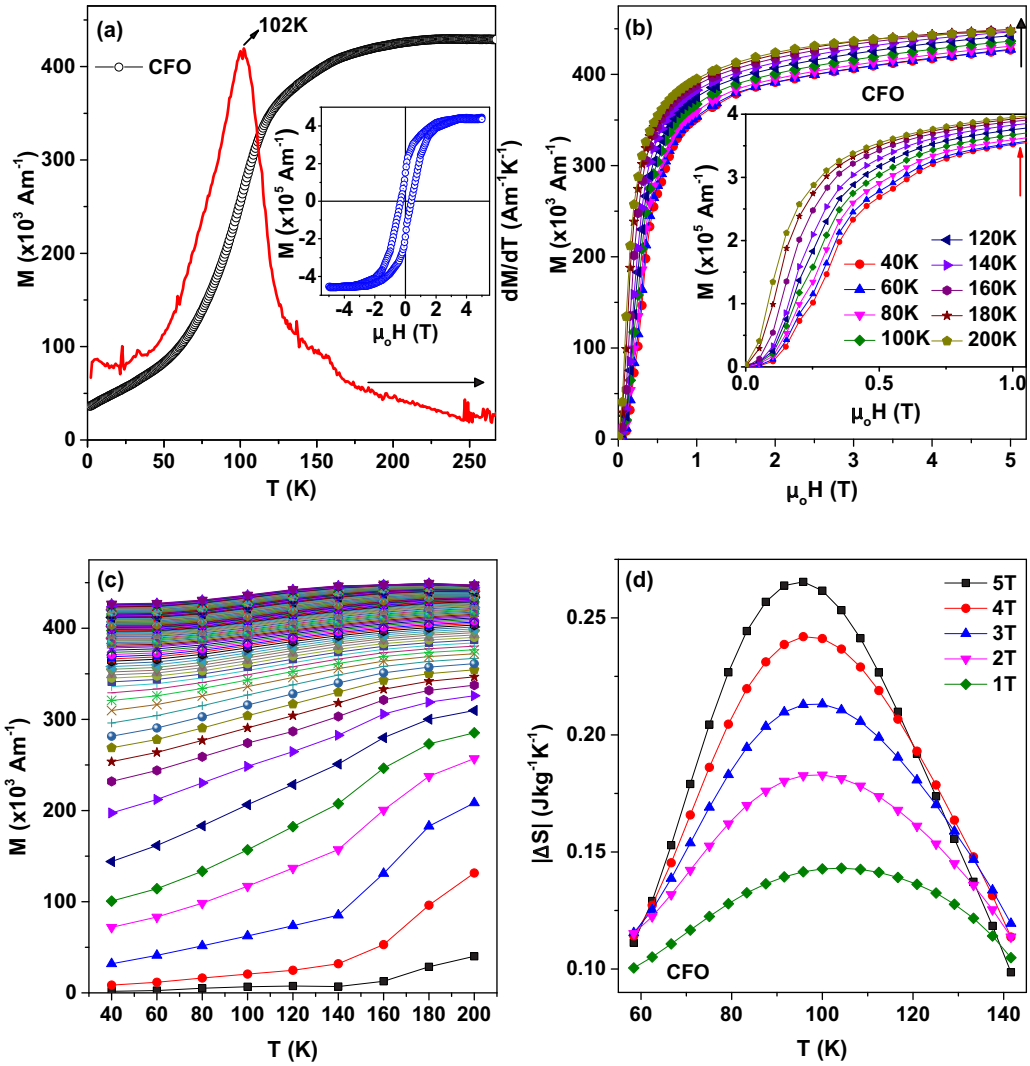

FIG. 6. (a) Temperature dependence of magnetization $M(T)$ and its derivative dM/dT for CFO thin film grown on MgO (100) substrate. Inset to (a) shows the magnetic hysteresis $M(H)$ loop at 300 K for single-layer CFO/MgO thin film. (b) Magnetic field dependence of magnetization $M(H)$ data at various temperatures from 40 to 200 K for CFO/MgO thin film. Inset to (b) shows the details of the $M(H)$ loops at low fields for single-layer CFO/MgO thin film. (c) Isothermal magnetization $M(T)$ curves at various magnetic fields from 0.05 to 5 T applied in regular intervals of 0.05 T for CFO/MgO thin film. (d) Temperature dependence of the magnetic-entropy change $|\Delta S|$ obtained under various fields from 1 to 5 T for CFO/MgO thin film.

dependent magnetization $M(T)$ curves as plotted in Fig. 6(c) for different fields starting from 0.05 to 5 T using Eq. (1). Figure 6(d) shows the $\Delta S(T)$ curves (from 1 to 5 T fields) for the CFO thin film. The maximum value of $|\Delta S|$ is 0.26 J kg^{-1}K^{-1} at 95 K for the highest field change of $|\Delta H| = 5$ T and $|\Delta S|$ is 0.14 J kg^{-1}K^{-1} at 100 K for the lowest field change of $|\Delta H| = 1$ T.

Figure 7(a) shows the temperature dependence of the zero-field-cooled (ZFC) and field-cooled (FC) magnetization $M(T)$ for CFO/LSMO heterostructure measured along the in-plane direction under an applied magnetic field of 0.05 T in the temperature range of 320 to 4 K. From the figure it is observed that the ZFC and FC curves almost coincide at high temperatures (250–300 K) but diverge with decreasing temperatures with a distinct magnetic phase transition at a temperature of 79 K as determined from the dM/dT vs T curves [shown in inset (I) to Fig. 7(a) for ZFC and FC curves]. This transition coincides and reconfirms the observed Verwey transition [50] in the CFO layer in CFO/LSMO since similar $M(T)$ curves measured for single-layer LSMO thin film [as shown in inset (II) to Fig. 7(a)] do not exhibit any feature of magnetic transition behavior in the chosen temperature range. The $M(T)$ curves measured for CFO/LSMO at a lower magnetic field of 0.005 T also exhibit comparable behavior (see Fig. S5 in the Supplemental Material [67]). Furthermore, the $T_V \approx 79$ K matches with the transition observed from the temperature dependent XRD analyses discussed in Figs. 4(a) and 4(b). Commercially bought bulk CFO powders (used for the preparation of the PLD target) exhibited the T_V at ≈90 K similar to earlier bulk report [50] (see Fig. S4 in the Supplemental Material [67]). However, the $M(T)$ curves for CFO/LSMO are completely different from both the bulk CFO powder or reported single-layer epitaxial ferrite (Fe_3O_4) thin films on MgO where during cooling a sharp drop in magnetization from M_{sat} to almost zero

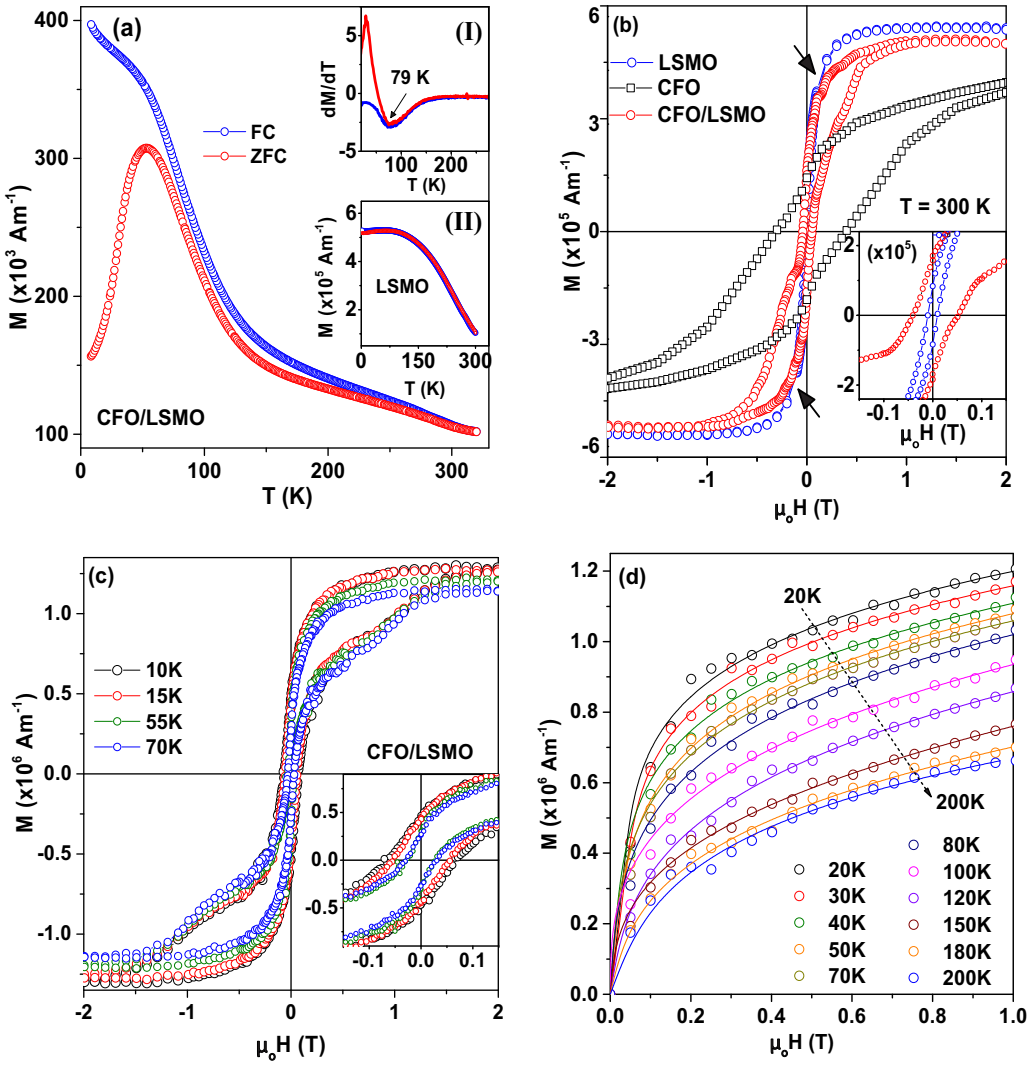

FIG. 7. (a) Temperature dependence of magnetization $M(T)$ taken for both zero-field cooled (ZFC) and field cooled (FC) at 0.05 T applied magnetic field for CFO/LSMO/MgO heterostructure. Inset (I) to (a) dM/dT of ZFC and FC curves for CFO/LSMO/MgO heterostructure. Inset (II) to (a) shows temperature dependence of magnetization $M(T)$ taken for ZFC and FC at 0.05 T for single-layer LSMO/MgO thin film. (b) Magnetic hysteresis $M(H)$ loops at 300 K for single-layer LSMO/MgO and bilayer CFO/LSMO/MgO heterostructure. Inset (I) to (b) shows details of the $M(H)$ curves for LSMO/MgO and CFO/LSMO/MgO at low fields. (c) $M(H)$ loops at different temperatures of 10, 15, 55, and 70 K for CFO/LSMO/MgO heterostructure. Inset to (c) shows the details of the $M(H)$ loops at low fields. (d) Magnetic field dependence of magnetization $M(H)$ data at various temperatures from 20 to 200 K for CFO/LSMO/MgO heterostructure.

magnetization is observed in a narrow range of temperature of 10–12 K across the first-order Verwey transition temperature [55,57,74]. Interestingly, in case of our epitaxial CFO/LSMO heterostructure, the magnetization does not drop to zero about the T_V but rather increases with decreasing temperature as in the FC curve in Fig. 7(a). Also, in the ZFC curve there is a clear indication of a magnetic transition near $T_V \sim 79$ K, which could be most likely attributed to the ferrimagentic, transition in CFO. The slightly lower T_V ($\approx$79 K) observed in CFO/LSMO than that observed for bulk CFO powders ($T_V \approx 90$ K) (Fig. S4 in the Supplemental Material [67]) could be attributed to the epitaxial compressive strain in the CFO layer within CFO/LSMO (as evidenced from the XRD analyses) heterostructure. Shift in T_V to lower values than in bulk samples could be attributed to compressive strain in epitaxial ferrite thin films as in a previous report [55].

Figure 7(b) are the in-plane $M(H)$ hysteresis curves at 300 K for CFO/LSMO and single-layer LSMO and CFO thin films. From Fig. 7 it is clearly seen that saturation magnetization in CFO/LSMO ($M_S = 533 \pm 10$ kA m^{-1}) is nearly same as that of the single-layer LSMO film ($M_S = 540 \pm 6$ kA m^{-1}), while the latter is in good agreement with previously reported values of epitaxial LSMO films [66,75,76]. However, there is four times enhancement of the coercive field in CFO/LSMO ($H_c = 0.0455$ T) as compared to LSMO ($H_c = 0.01$ T) as shown in the detailed view in inset (I) to Fig. 7(b). This is a direct consequence of the incorporation of the hard-magnetic CFO layer in the CFO/LSMO

heterostructure [76]. As shown in Fig. 7(b), the single-layer CFO film on MgO substrate exhibits much larger coercive field ($H_c = 0.35\,\mathrm{T}$) and a magnetization of $413\,\mathrm{kA\,m^{-1}}$ at 2 T field at 300 K which is almost 30% less than that of CFO/LSMO at similar fields. The enhanced magnetization of CFO/LSMO as compared to the single-layer CFO film as shown in Fig. 7(b) can be attributed to the combined influence of the interfacial magnetic coupling and stress. In a magnetostrictive material like CFO, the effect of stress (σ) on magnetization (M) can be understood from the following thermodynamic relation [77]:

$$\frac{1}{l}\frac{\partial l}{\partial H} = \frac{\mu_o}{4\pi}\frac{\partial M}{\partial \sigma}, \tag{3}$$

where μ_o is the permeability of free space, and $\partial l/l$ is the magnetostriction of the material under application of external applied magnetic field (H). From Eq. (3) the in-plane magnetization in CFO, a negative magnetostrictive material (i.e., $\Delta l/l < 0$), will be increased by in-plane compressive stress (i.e., $\partial\sigma < 0$), and decreased by in-plane tensile stress (i.e., $\partial\sigma < 0$).). Since the in-plane stress (σ_{par}) is related to in-plane strain ($\varepsilon_{\mathrm{par}}$) by the relation $\sigma_{\mathrm{par}} = Y\varepsilon_{\mathrm{par}}$ (where $Y =$ Young's modulus of CFO, $Y_{100} = 1.5\times10^{11}\,\mathrm{N\,m^{-2}}$) it is clear that the magnetization of CFO is affected by in-plane epitaxial strain. From the XRD strain analysis of strain, we can observe that the CFO layer in CFO/LSMO is under in-plane compressive stress ($\sigma_{\mathrm{par}} = Y_{100}\varepsilon_{\mathrm{par}} = -6\times10^{8}\,\mathrm{N\,m^{-2}}$). On the other hand, the CFO layer in the single-layer CFO film on MgO is under in-plane tensile stress ($\sigma_{\mathrm{par}} = Y_{100}\varepsilon_{\mathrm{par}} = 1.5\times10^{8}\,\mathrm{N\,m^{-2}}$). The different stresses in the CFO layer in CFO/LSMO and CFO thin film explains the lower magnetization in CFO thin film as compared to CFO/LSMO.

An interesting feature of the $M(H)$ loop for CFO/LSMO is a distinct constricted hysteresis nature at low fields which is absent in the single-layer LSMO and CFO films. From Fig. 7(b) it is clear that the magnetic hysteresis for CFO-LSMO is quite different from that of the LSMO and CFO single-layered thin films which indicates the coupling of the CFO and LSMO layers in the heterostructure. Such constricted hysteresis loops are typically observed in many composite ferroic systems consisting of two different magnetic phases with high and low coercivities [78,79]. The constricted behavior is enhanced at low temperatures as evident from the $M(H)$ loops at different temperatures of 10, 15, 55, and 70 K for CFO/LSMO heterostructure shown in Fig. 7(c). All these results indicate that a clear enhancement of the magnetization is achieved at low fields in the CFO/LSMO heterostructure as compared to the single-layer CFO thin film, which otherwise increases its efficacy as a MC composite system. Figure 7(d) shows the isothermal magnetization $M(H)$ curves measured for 1 T fields for various temperatures starting from 200 to 20 K. The virgin $M(H)$ curves measured at various temperatures were used to calculated the MC properties for the CFO/LSMO heterostructure.

In order to evaluate the MC behavior of CFO/LSMO, the temperature dependent magnetization $M(T)$ curves are plotted in Fig. 8(a) for different fields starting from 0.05 to 1 T (in steps of 0.05 T as shown with the arrow). From Fig. 8 it is evident that the magnetization decreases quite gradually with increasing temperature, which is otherwise an indicative of a second-order type phase transition. This is absent in polycrystalline ferrite bulk and thin films where first-order Verwey transitions are observed [60]. Moreover, the proposed second-order phase transition temperature shifts to higher values at larger applied fields due to the field induced magnetostructural transitions at high fields. In order to further investigate the nature of the magnetic transition the $M(H)$ data were fitted to the Ginzburg-Landau mean field theory for magnetism where the magnetic free energy, $F(M,H)$ can be expressed as [80,81]

$$F(H,M) = \tfrac{1}{2}a(T)M^2 + \tfrac{1}{4}b(T)M^4 + \tfrac{1}{6}c(T)M^6 - \mu_o HM, \tag{4}$$

where $a(T)$, $b(T)$, and $c(T)$ are the material constants. Close to the phase transition, the condition for minimization of free energy gives

$$a(T)M + b(T)M^3 + c(T)M^5 = \mu_o H, \tag{5}$$

where $a(T)$, $b(T)$, and $c(T)$ can be determined by fitting the isothermal magnetization data using Eq. (5) (as shown in Fig. S6(a) in the Supplemental Material [67]). From the mean field model the conditions that determine if a phase transition is second-order are

for $T < T_C$, $a(T) > 0$, $b(T) < 0$, and $c(T) > 0$,

for $T > T_C$, $a(T) > 0$, $b(T) > 0$, and $c(T)$ is <0 or > 0.

The coefficients $a(T)$, $b(T)$, and $c(T)$ as shown in Figs. S6(b)–S6(d) in the Supplemental Material [67] are consistent with the above conditions implying that there is indeed a second-order type magnetic transition present in CFO/LSMO heterostructure thin film [80,81]. These criteria for second-order phase transition is further shown as M^2 vs H/M isotherms plots (Arrot plots) in Fig. 8(b) at various temperatures from 200 to 20 K. According to the Banerjee criterion [82] for phase transition, the positive slopes of the Arrot plots as shown in Fig. 8(b) suggest that the magnetic phase transition is second-order type in nature. Furthermore, since the plot of the M^2 vs H/M data for 80 K passes through the origin, it indicates a $T_C \approx 80\,\mathrm{K}$ for the CFO/LSMO heterostructured system, which is close to that observed from the XRD analyses discussed. Figure 8(c) shows the temperature dependence of entropy change $\Delta S(T)$ for CFO/LSMO for field variation up to 1 T as calculated using the thermodynamical Maxwell's equation (1). The $\Delta S(T)$ curves are found to be broad over a large range of temperature due to the second-order-like magnetic phase transition as confirmed from the $M(T)$ curves in Fig. 8(a). The maximum value of $|\Delta S|$ is $0.63\,\mathrm{J\,kg^{-1}K^{-1}}$ at $T_V = 80\,\mathrm{K}$ for a field change of $|\Delta H| = 1\,\mathrm{T}$; much higher than the CFO thin film ($|\Delta S| = 0.14\,\mathrm{J\,kg^{-1}}$ at $T_V = 102\,\mathrm{K}$) and that reported for CFO nanoparticles ($0.05 < |-\Delta S| < 0.23$) under similar field changes of $|\Delta H| = 1\,\mathrm{T}$ [83,84], which might be primarily due an order of magnitude higher magnetization of CFO/LSMO around the T_V (80 K) as compared to that in the CFO thin film as shown in the $M(T)$ curves in Figs. 6(c) and 8(a). The MC entropy change for CFO/LSMO at higher fields up to 5 T was also evaluated following similar analyses of field and temperature dependent magnetization measurements (as shown in Fig. S7 in the Supplemental Material [67]). The $\Delta S(T)$ curves are broad between room temperature and 200 K; and the highest entropy change $|\Delta S|$ is $3.8\,\mathrm{J\,kg^{-1}K^{-1}}$

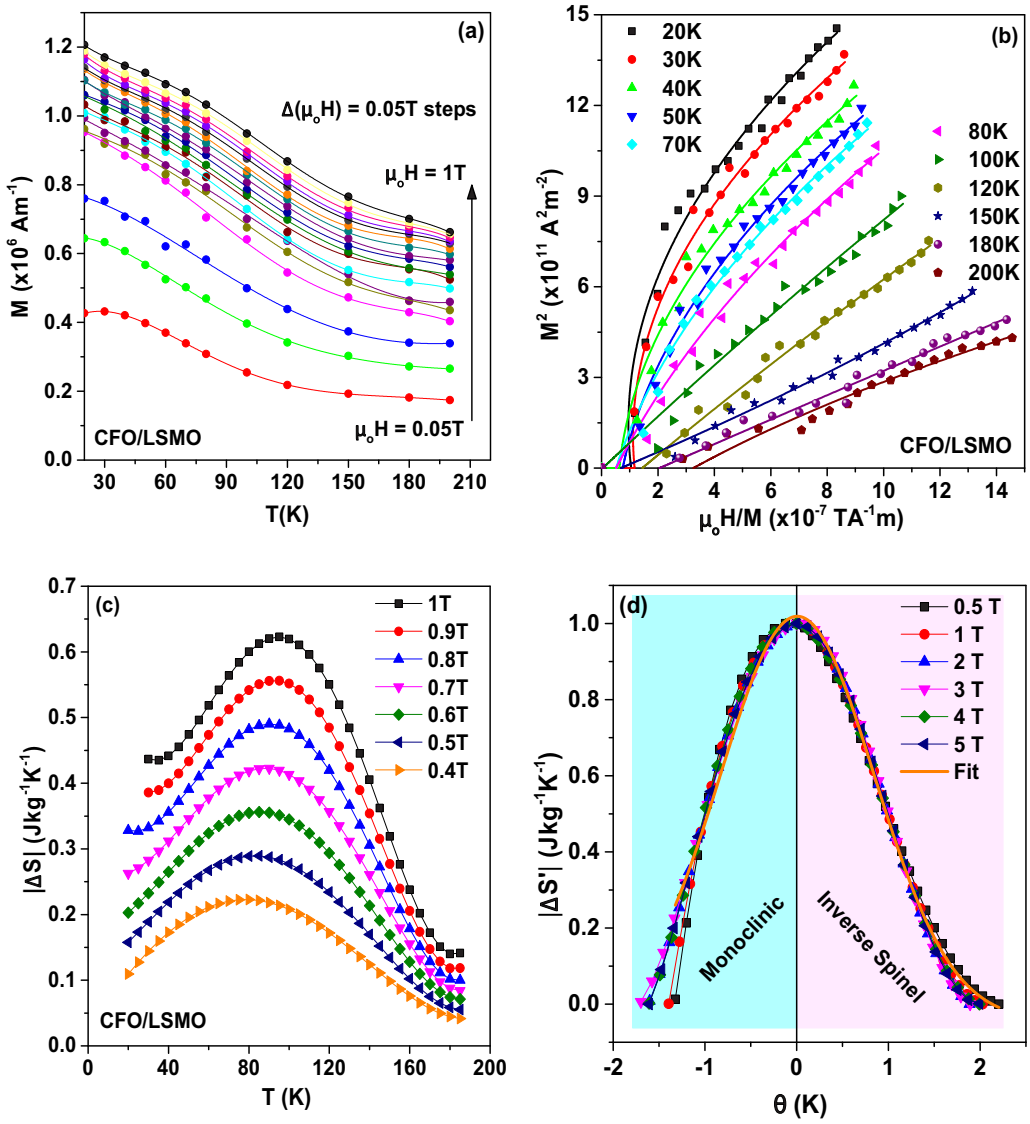

FIG. 8. (a) Isothermal magnetization $M(T)$ curves at various magnetic fields from 0.05 to 1 T applied in regular intervals of 0.05 T for CFO/LSMO/MgO heterostructure. The direction of increasing applied fields is marked by an arrow. (b)The M^2 vs H/M plots (Arrot plots) of the isotherms in (a). (c) Temperature dependence of the magnetic-entropy change $|\Delta S|$ obtained under various fields from 0.4 to 1 T for CFO/LSMO/MgO heterostructure. (d) Universal curve of normalized entropy change $|\Delta S'|$ versus rescaled temperature θ for different magnetic field from 0.5 to 5 T for the CFO/LSMO/MgO heterostructure. The regions marked with blue and pink are the monoclinic (or nearly tetragonal) and inverse spinel phases of CFO.

for a field change of $|\Delta H| = 5$ T at a transition temperature of ~102 K. Since we attribute the broadness of the $\Delta S(T)$ curves to the second-order type phase transition in CFO/LSMO, which is uncharacteristic of the first-order Verwey transition in bulk ferrites, we used the phenomenological universal curve method, proposed by Franco *et al.* [85–87]. This is a general approach to determine the order of the phase transition as an alternative to the Banerjee criterion [82] used in Fig. 8(b). The theoretical justification of this procedure [88] implies that if all $\Delta S(T)$ curves obtained at different fields collapse onto a single universal curve when appropriately normalized and rescaled, the magnetic phase transition is of second-order in nature [85–87]. Following this postulation, the universal curve is constructed by normalizing the $\Delta S(T)$ curves at different fields with their maximum values [i.e., $\Delta S' = \Delta S(T)/\Delta S_{\max}(T)$] and rescaling the temperature axis as [85–87]

$$\theta = \begin{cases} -(T - T_C)/(T_{R_1} - T_C), & T \leqslant T_C, \\ (T - T_C)/(T_{R_2} - T_C), & T > T_C, \end{cases} \tag{6}$$

where T_{R_1} and T_{R_2} are the two reference temperatures corresponding to the half-maximum of $\Delta S(T_{R_1}) = \Delta S(T_{R_2}) = \Delta S(T_C)/2$. It is interesting to note that, using the phenomenological construction of the universal curve, all the normalized $\Delta S'(T)$ curves at fields from 0.5 to 5 T (as shown in Fig. S7(c) in the Supplemental Material [67]) for the CFO/LSMO heterostructure collapse onto a single curve in Fig. 8(d). The inverse spinel and monoclinic phases

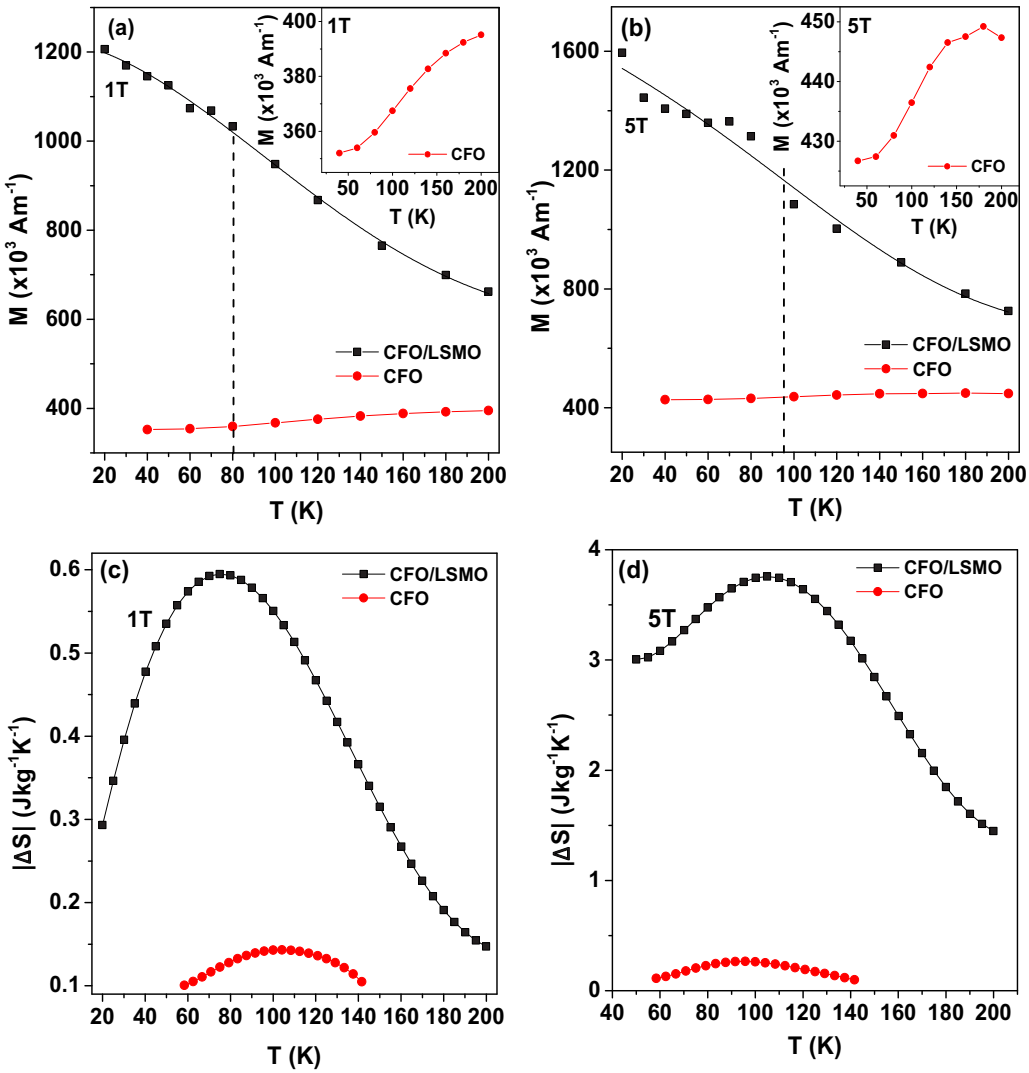

FIG. 9. Temperature dependence of magnetization $M(T)$ curves measured at applied fields of (a) 1 T and (b) 5 T for CFO/MgO thin film and CFO/LSMO/MgO heterostructure, respectively. The insets to (a) and (b) show the zoomed in view of the $M(T)$ curves for the CFO/MgO thin film. The vertical dotted lines show the Verwey transition temperatures (T_V) for CFO/LSMO/MgO heterostructure for the different fields. It is clearly visible that around the Verwey transition temperatures the magnetization of CFO/LSMO/MgO is 188% enhanced for 1 T and 200% enhanced for 5 T fields, respectively. Temperature dependence of magnetic-entropy change $|\Delta S|$ curves at applied fields of (c) 1 T and (d) 5 T for CFO/MgO thin film and CFO/LSMO/MgO heterostructure, respectively.

(nearly tetragonal; $a \approx b < c$, $\alpha = 90.2°$, $\beta = \gamma = 90°$, $\beta = \gamma = 90°$) of CFO are marked with different colors in Fig. 8. This reconfirms the presence of a unique second-order magnetic phase transition in a CFO/LSMO thin film heterostructured system. This analysis is also consistent with the trends observed in the Arrott plots in Fig. 8(b). As the reason for this unusual second-order Verwey transition in our magnetic materials system as opposed to the first-order transition observed in bulk ferrites, we believe that it might be artificially induced due to the highly strained CFO layer in CFO/LSMO heterostructure. Based on the calculations of magnetic entropy change $|\Delta S|$ using the data obtained from the magnetic measurements, we observe a huge enhancement in MC entropy change in CFO/LSMO heterostructure ($|\Delta S| = 3.8\,\mathrm{J\,kg^{-1}K^{-1}}$ at $|\Delta H| = 5\,\mathrm{T}$ around $T_V = 102\,\mathrm{K}$) as compared to that of the CFO thin film ($|\Delta S| = 0.26\mathrm{J\,kg^{-1}K^{-1}}$ at $|\Delta H| = 5\,\mathrm{T}$ around $T_V = 95\,\mathrm{K}$) shown in Fig. 6(d). It is concluded that the primary reason for the enhancement of MC entropy change in CFO/LSMO as compared to CFO thin film is due to an order of magnitude increased magnetization in CFO/LSMO as compared to CFO at around the T_V as shown in Figs. 9(a) and 9(b) for 1 and 5 T fields, respectively. In order to highlight the enhanced entropy change in CFO/LSMO as compared to CFO, the $\Delta S(T)$ curves have been shown in the same plots in Figs. 9(c) and 9(d) for 1 and 5 T fields, respectively (see Table II).

Besides the Arrott plots in combination with the Banerjee criterion [Fig. 8(b)] and the universal curve method [Fig. 8(d)] we use another quantitative criterion for the unambiguous determination of the order of magnetic phase transition in CFO/LSMO/MgO heterostructure using the approach proposed by Law *et al.* [25]. In this process we determine the

TABLE II. Comparison of magnetic and magnetocaloric characteristics of CFO/MgO and CFO/LSMO/MgO heterostructures: saturation magnetization (M_S) and coercivity (H_c) at 300 K, Verwey transition temperature (T_V), isothermal entropy change $|\Delta S|$(J kg^{-1}K^{-1}) for low field (1 T) and high field (5 T) around T_V.

Sample	M_s(kA m^{-1})	$H_c(T)$	T_V (K)	$\lvert\Delta S\rvert$(J kg^{-1}K^{-1}) for 1 T	$\lvert\Delta S\rvert$(J kg^{-1}K^{-1}) for 5 T
CFO/MgO	443 ± 13	0.35	102	0.14	0.26
CFO/LSMO/MgO	533 ± 10	0.0455	79	0.63	3.8

model-independent exponent (n) from the field dependence of the magnetic entropy change $|\Delta S|$ [25] which is represented as a power law of the field H as

$$|\Delta S| \propto H^n, \tag{7}$$

with an exponent n that is dependent on field and temperature. It can be locally calculated as [89]

$$n(T, H) = \frac{d\ln|\Delta S|}{d\ln H}. \tag{8}$$

If the above analyses yields $n > 2$, then it confirms a first-order phase transition and if it yields $n < 2$ it implies a second-order phase transition. Figure 10(a) shows the three-dimensional plots of field and temperature dependence of the magnetic entropy change ($|\Delta S|$) as obtained from the magnetization measurements for CFO/LSMO/MgO heterostructure at a temperature range from 20 to 200 K under varying applied magnetic fields 0 to 5 T. From Fig. 10(a) it is observed that the MC surface exhibits a second-order phase transition with a "caret-type" behavior [25] showing that the temperature evolution of $|\Delta S|$ is gradual for all magnetic field values and likewise there is no abrupt change in the field dependence for any of the isotherms. Figure 10(b) shows the field and temperature dependence of the values of the exponent n for CFO/LSMO/MgO range from 20 to 200 K under varying applied magnetic fields 0 to 5 T. For the entire range of field and temperature the maximum value of n is 1.75 (i.e., $n < 2$) which confirms the second-order phase transition in CFO/LSMO, since for first-order phase transition the value is $n > 2$. The above analysis further supports the conjecture that the phase transition in CFO/LSMO is indeed second-order in nature.

Figure 11(a) schematically shows an idealized CFO/LSMO interface (i.e., without any chemical or structural imperfections) near room temperature with cube-on-cube epitaxial growth. The site occupancies of Fe and Co ions in the inverse spinel structure of the CFO layer shown in Fig. 11(a) has been assigned by considering the ideal inversion parameter for CFO in CFO/LSMO since XPS analyses provided a value of 0.94 which is close to 1. It is noted that Fig. 11(a) does not take into account the charge disproportionation at Fe sites or the site occupancy disorder which presumably appears at the Verwey transition. We also considered that the perovskite LSMO unit cell in CFO/LSMO heterostructure, as shown in Fig. 11(a), has FM order due to double-exchange interaction between Mn^{3+} and Mn^{4+} mediated by oxygen ions [90], while the inverse-spinel CFO unit cell has antiferromagnetic interaction between the Fe^{3+} ions at the tetrahedral and orthogonal sites via superexchange interactions mediated by oxygen ions [61]. Therefore, the uncompensated Co^{2+} moment gives long-range ferrimagnetic order in CFO. In Fig. 11(b) we illustrate the effect of interfacial lattice mismatch strains on the tetragonal distortion of the CFO unit cell in CFO/MgO and CFO/LSMO/MgO in comparison to the unstrained bulk CFO unit cell and the corresponding T_V observed in this work. The tetragonal distortion of the CFO unit cell due to interfacial strain may cause the canting of the Fe^{3+} and Co^{2+} moments shown in Fig. 11(a) and drastically change the magnetic properties in CFO/LSMO heterostructure [61,64]. Here we assume, at the interface of the CFO/LSMO, possible FM or anti-FM exchange coupling between the Fe^{3+}

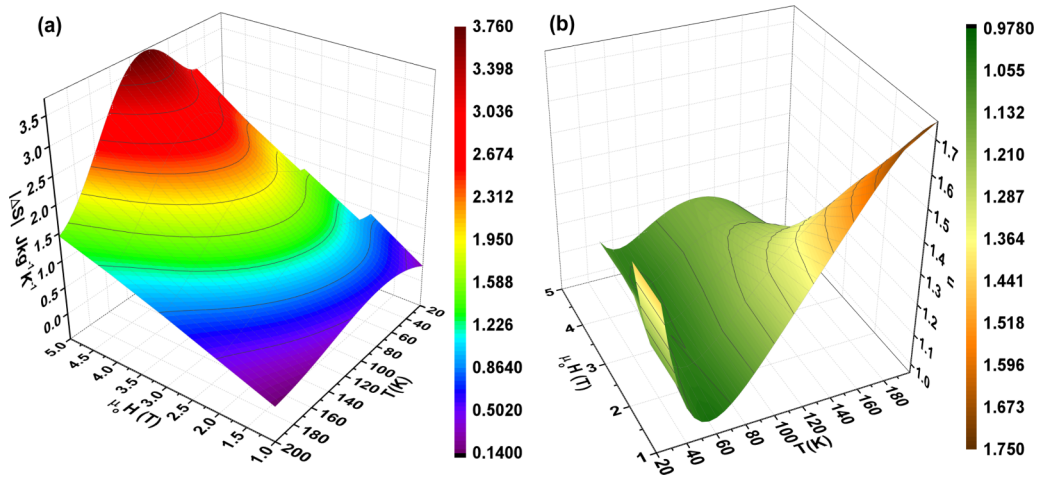

FIG. 10. Three-dimensional plots of field and temperature dependence of (a) magnetic entropy change ($|\Delta S|$) and (b) critical exponent of phase transition (n) for CFO/LSMO/MgO heterostructure at temperature range from 20 to 200 K under varying applied magnetic fields 0 to 5 T.

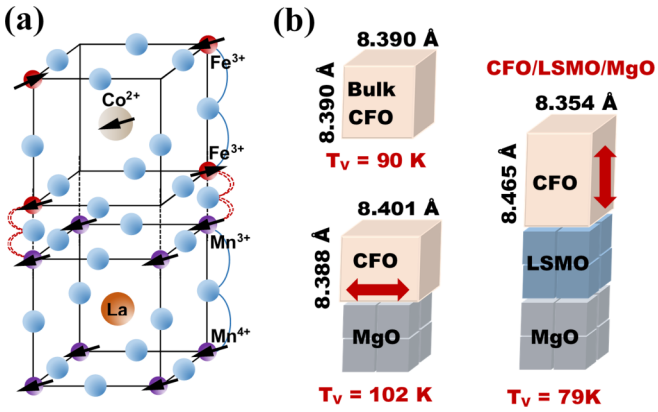

FIG. 11. (a) Schematic illustration of the atomic and spin configurations of the unit cells at the CFO/LSMO interface. (b). Schematic diagram illustrating the tetragonal distortion of the fcc bulk lattice ($a = 0.839$ nm) in the CFO/MgO and CFO/LSMO/MgO heterostructures. The in-plane and out-of-plane lattice parameters were calculated from XRD scans.

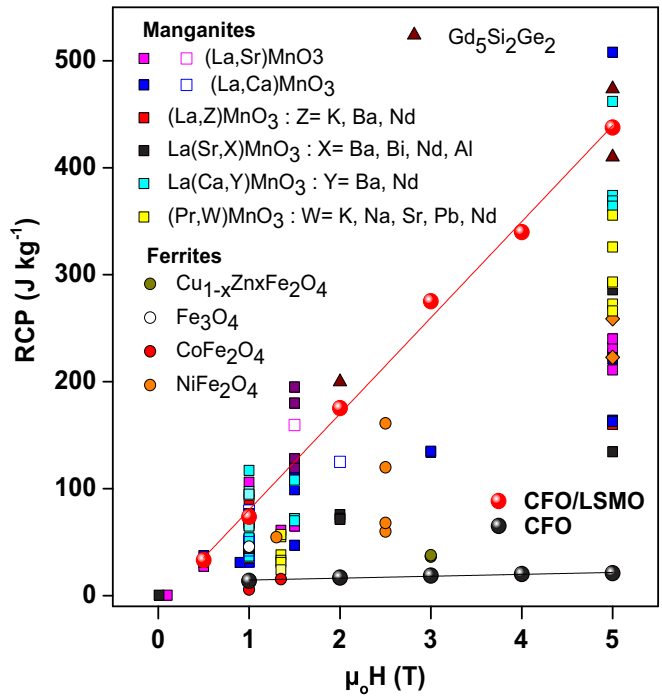

FIG. 12. Relative cooling power (RCP) values at different applied magnetic fields for a wide variety of MC materials from literature and the same obtained for CFO/LSMO/MgO heterostructure. Perovskite manganites and ferrites are denoted by different symbols. The solid and open symbols denote bulk and thin film values, respectively. The solid red line shows the linear fit of RCP values for CFO/LSMO for different fields.

and Mn^{3+} mediated by oxygen ions [shown by red dotted curves in Fig. 11(a)] could be present. One can speculate that these competing FM and anti-FM orders for the Fe-O-Mn exchange interactions at the CFO/LSMO interface may give rise to the different magnetic behaviors under different field and temperature conditions as compared to CFO/MgO thin film where there are no such Fe-O-Mn exchange interactions. We propose that in the highly strained epitaxial CFO/LSMO heterostructure, there could be pinning of magnetic moments of the CFO and LSMO at the CFO/LSMO interface generated due to the strain coupling of these two phases. This might lead to the observed second-order type magnetic transition and enhanced MC properties in our heterostructured system.

Finally, the relative cooling power (RCP) values at different fields for the CFO/LSMO heterostructure were calculated using Eq. (2) which were found to increase linearly with field from RCP at 1 T = 73.6 J kg^{-1} to RCP at 5 T = 437.6 J kg^{-1} as shown in Fig. 12. It is to be noted that the effect of substrate is neglected during the calculation of RCP values since the the magnetization data are corrected for the diamagnetic contribution from the MgO substrate [58–62]. From an exhaustive literature survey, we calculated the RCP values [using Eq. (2)] of traditional MC materials such as perovskite manganites and ferrites, which are plotted in Fig. 12 as a function of the magnetic fields. From Fig. 12 it is clearly observed that the RCP values for CFO/LSMO are much higher than the CFO thin film in our work and also ferrite nanoparticles or polycrystalline thin films of Fe_3O_4 (RCP = 45.8 J kg^{-1} at 1 T) [60], $CoFe_2O_4$ (RCP = 15.4J kg^{-1} at 1 T) [84], $NiFe_2O_4$ (RCP = 60J kg^{-1} at 2.5 T) [91], $Cu_xZn_{1-x}Fe_2O_4$ (RCP = 36.7 J kg^{-1} at 3 T) [92], $Ni_xZn_{1-x}Fe_2O_4$ (RCP = 54.6J kg^{-1} at 1 T) [93] so far reported in literature. In fact, the RCP value of CFO/LSMO heterostructure is comparable to the celebrated MC material $Gd_5Si_2Ge_2$ which makes CFO/LSMO magnetic system highly attractive for MC applications. Since consisting of all oxide components, it is also likely to be more stable under normal conditions as opposed to the unstable $Gd_5Si_2Ge_2$. It is to be noted that both magnetic and thermal hysteresis could compromise the RCP values in CFO/LSMO/MgO. We have observed from the heating and cooling cycles of the calculated lattice parameters from XRD [Fig. S3(b)] [67] and conductivity (Fig. 5) measurements that there is no detectable thermal hysteresis in CFO/LSMO/MgO which is attributed to the second-order type transition around the T_V in the heterostructure. Thus, thermal hysteresis losses do not affect the RCP values in CFO/LSMO/MgO. However, RCP values at different fields for CFO/LSMO/MgO and CFO/MgO as shown in Fig. 12 could be compromised by the magnetic hysteresis losses [see $M(H)$ loop in Fig. 7(b)]. We have calculated the magnetic hysteresis loss from the area under the $M(H)$ loop for CFO/LSMO/MgO in Fig. 7(b) which is 39.4J kg^{-1}. This is almost 10 times smaller than the RCP value of 437.6 J kg^{-1} at 5 T for CFO/LSMO/MgO. Thus, due to the magnetic hysteresis losses, the RCP value could be only slightly compromised in CFO/LSMO/MgO. In comparison, for CFO/MgO thin film the area under the $M(H)$ loop in Fig. 7(b) is 128.4J kg^{-1} which is quite large and will drastically reduce the RCP value for CFO thin film. This further highlights the efficacy of CFO/LSMO/MgO for enhanced MC effects as compared to CFO/MgO thin film. The enhanced RCP observed in CFO/LSMO is plausibly due to the magnetostructural coupling and consequently second-order type phase transition in the system as have been discussed in detail. In general, this kind of structural engineering of magnetic phases could lead to the realization of many other novel MC structures with improved functionalities for developing next generation solid state cooling technology.

IV. CONCLUSIONS

In summary, we studied the structural, magnetic, and magnetocaloric properties of CFO/LSMO heterostructure and CFO thin film grown on MgO (100) substrate using an optimized PLD technique. Detailed room temperature XRD along with different microscopic image analyses indicated high quality single crystalline and epitaxial growth of the individual material layers. Temperature dependent XRD studies reveal a structural phase transition ∼80 K, attributed to the Verwey transition of CFO. Detailed analyses of magnetic properties reveal it rather as a second-order phase transition, which is confirmed by structural studies. Thermodynamic calculations reveal a maximum entropy change of $\sim 0.622\,\mathrm{J\,kg^{-1}K^{-1}}$ with relative cooling power (RCP) of $73.6\mathrm{J\,kg^{-1}}$ in a magnetic variation of 1 T that instate the potential of the CFO/LSMO/MgO thin film as a promising candidate for magnetic refrigeration at low temperatures. We strongly believe that interfacial strain-induced magnetostructural coupling of the CFO layer with the underlying LSMO layer gives rise to these hitherto unobserved enhanced magnetocaloric effects in the heterostructure thin film, which has been supported by theoretical calculations.

ACKNOWLEDGMENTS

D.M. acknowledges the funding from the Technical Research Center, Department of Science and Technology, Government of India (Grant No. AI/1/62/IACS/2015) and Science and Engineering Research Board (SERB), Government of India (Grant No. SRG/2019/000387). A.D. acknowledges funding from Ramanujan Fellowship, Science and Engineering Research Board (SERB), Government of India (Award No. SB/S2/RJN-057/2017).

D.M. and A.D. conceptualized the work and designed the synthesis. A.B. and S.C. performed the experiments and collected the data. J.D. helped in the magnetic work and data collection. D.M. and A.B. analyzed the data. A.B., A.D., and D.M. cowrote the paper.

[1] X. Moya, S. Kar-Narayan, and N. D. Mathur, Nat. Mater. **13**, 439 (2014).
[2] A. Barman, S. Kar-Narayan, and D. Mukherjee, Adv. Mater. Interfaces **6**, 1900291 (2019).
[3] O. Gutfleisch, M. A. Willard, E. Brück, C. H. Chen, S. G. Sankar, and J. P. Liu, Adv. Mater. **23**, 821 (2011).
[4] B. F. Yu, Q. Gao, B. Zhang, X. Z. Meng, and Z. Chen, Int. J. Refrig. **26**, 622 (2003).
[5] K. A. Gschneidner, Jr., V. K. Pecharsky, and A. O. Tsokol, Rep. Prog. Phys. **68**, 1479 (2005).
[6] A. Smith, C. R. H. Bahl, R. Bjørk, K. Engelbrecht, K. K. Nielsen, and N. Pryds, Adv. Energy Mater. **2**, 1288 (2012).
[7] G. V. Brown, J. Appl. Phys. **47**, 3673 (1976).
[8] A. Kitanovski and P. W. Egolf, Int. J. Refrig. **33**, 449 (2010).
[9] C. R. H. Bahl, T. F. Petersen, N. Pryds, and A. Smith, Rev. Sci. Instrum. **79**, 093906 (2008).
[10] M. Ghahremani, A. Aslani, M. Hosseinnia, L. H. Bennett, and E. D. Torre, AIP Adv. **8**, 056426 (2018).
[11] K. A. Gschneidner, Jr. and V. K. Pecharsky, Annu. Rev. Mater. Sci. **30**, 387 (2000).
[12] J. Liu, T. Gottschall, K. P. Skokov, J. D. Moore, and O. Gutfleisch, Nat. Mater. **11**, 620 (2012).
[13] V. K. Pecharsky and K. A. Gschneidner, Jr., Phys. Rev. Lett. **78**, 4494 (1997).
[14] J. D. Moore, K. Morrison, G. K. Perkins, D. L. Schlagel, T. A. Lograsso, K. A. Gschneidner, Jr., V. K. Pecharsky, and L. F. Cohen, Adv. Mater. **21**, 3780 (2009).
[15] H. Wada and Y. Tanabe, Appl. Phys. Lett. **79**, 3302 (2001).
[16] A. Yan, K.-H. Müller, L. Schultz, and O. Gutfleisch, J. Appl. Phys. **99**, 08K903 (2006).
[17] A. Fujita, S. Fujieda, Y. Hasegawa, and K. Fukamichi, Phys. Rev. B **67**, 104416 (2003).
[18] O. Tegus, E. Brück, K. H. J. Buschow, and F. R. de Boer, Nature (London) **415**, 150 (2002).
[19] T. Samanta, I. Das, and S. Banerjee, Appl. Phys. Lett. **91**, 152506 (2007).
[20] L. Li, K. Nishimura, W. D. Hutchison, Z. Qian, D. Huo, and T. NamiKi, Appl. Phys. Lett. **100**, 152403 (2012).
[21] C. R. H. Bahl, D. Velazquez, K. K. Nielsen, K. Engelbrecht, K. B. Andersen, and R. Bulatova, N. Pryds Appl. Phys. Lett. **100**, 121905 (2012).
[22] K. Ahn, V. K. Pecharsky, and K. A. Gschneider, Jr., J. Appl. Phys. **106**, 043918 (2009).
[23] A. C. Sackville Hamilton, G. I. Lampronti, S. E. Rowley, and S. E. Dutton, J. Phys.: Condens. Matter **26**, 116001 (2014).
[24] X. Moya, E. Defay, V. Heine, and N. D. Mathur, Nat. Phys. **11**, 202 (2015).
[25] J. Y. Law, V. Franco, L. M. Moreno-Ramírez, A. Conde, D. Y. Karpenkov, I. Radulov, K. P. Skokov, and O. Gutfleisch, Nat. Commun. **9**, 2680 (2018).
[26] A. Giguère, M. Foldeaki, B. Ravi Gopal, R. Chahine, T. K. Bose, A. Frydman, and J. A. Barclay, Phys. Rev. Lett. **83**, 2262 (1999).
[27] M. Pasquale, C. P. Sasso, L. H. Lewis, L. Giudici, T. Lograsso, and D. Schlagel, Phys. Rev. B **72**, 094435 (2005).
[28] T. D. Thanh, D. C. Linh, P. D. H. Yen, L. V. Bau, V. H. Ky, Z. Wang, H. G. Piao, N. M. An, and S. C. Yu, Physica B **532**, 166 (2018).
[29] C. W. Miller, D. D. Belyea, and B. J. Kirby, J. Vacuum Sci. Technol. A **32**, 040802 (2014).
[30] V. G. Prokhorov, V. A. Komashko, G. G. Kaminsky, K. K. Yu, S. J. Jun, S. Y. Park, J. S. Park, Y. P. Lee, and V. L. Svetchnikov, Low Temp. Phys. **33**, 58 (2007).
[31] D. T. Morelli, A. M. Mance, J. V. Mantese, and A. L. Micheli, J. Appl. Phys. **79**, 373 (1996).
[32] V. Recarte, J. I. Pérez-Landazábal, V. Sánchez-Alárcos, V. A. Chernenko, and M. Ohtsuka, Appl. Phys. Lett. **95**, 141908 (2009).
[33] T. Mukherjee, S. Sahoo, R. Skomski, D. J. Sellmyer, and Ch. Binek, Phys. Rev. B **79**, 144406 (2009).
[34] Q. Zhang, S. Thota, F. Guillou, P. Padhan, V. Hardy, A. Wahl, and W. Prellier, J. Phys.: Condens. Matter **23**, 052201 (2011).
[35] S. Thota, Q. Zhang, F. Guillou, U. Lüders, N. Barrier, W. Prellier, A. Wahl, and P. Padhan, Appl. Phys. Lett. **97**, 112506 (2010).

[36] R. Skomski, C. Binek, S. Michalski, T. Mukherjee, A. Enders, and D. J. Sellmyer, J. Appl. Phys. **107**, 09A922 (2010).

[37] L. E. Hueso, P. Sande, D. R. Miguéns, J. Rivas, F. Rivadulla, and M. A. López-Quintela, J. Appl. Phys. **91**, 9943 (2002).

[38] N. S. Bingham, A. K. Suszka, C. A. F. Vaz, H. Kim, and L. J. Heyderman, Phys. Rev. B **96**, 024419 (2017).

[39] X. Zhang, J. B. Wang, B. Li, X. L. Zhong, X. J. Lou, and Y. C. Zhou, J. Appl. Phys. **109**, 126102 (2011).

[40] C. W. Miller, D. V. Williams, N. S. Bingham, and H. Srikanth, J. Appl. Phys. **107**, 09A903 (2010).

[41] D. Matte, M. de Lafontaine, A. Ouellet, M. Balli, and P. Fournier, Phys. Rev. Appl. **9**, 054042 (2018).

[42] F. Johnson and R. D. Shull, J. Appl. Phys. **99**, 08K909 (2006).

[43] V. S. Kumar, R. Chukka, Z. Chen, P. Yang, and L. Chen, AIP Adv. **3**, 052127 (2013).

[44] M. Oumezzine, A. C. Galca, I. Pasuk, C. F. Chirila, A. Leca, V. Kuncser, L. C. Tanase, A. Kuncser, C. Ghica, and M. Oumezzine, Dalton Trans. **45**, 15034 (2016).

[45] S. N. Vdovichev, N. I. Polushkin, I. D. Rodionov, V. N. Prudnikov, J. Chang, and A. A. Fraerman, Phys. Rev. B **98**, 014428 (2018).

[46] X. Moya, L. E. Hueso, F. Maccherozzi, A. I. Tovstolytkin, D. I. Podyalovskii, C. Ducati, L. C. Phillips, M. Ghidini, O. Hovorka, A. Berger, M. E. Vickers, E. Defay, S. S. Dhesi, and N. D. Mathur, Nat. Mater. **12**, 52 (2012).

[47] T. E. Quickel, V. H. Le, T. Brezesinski, and S. H. Tolbert, Nano Lett. **10**, 2982 (2010).

[48] C. Schmitz-Antoniak, D. Schmitz, P. Borisov, F. M. F. de Groot, S. Stienen, A. Warland, B. Krumme, R. Feyerherm, E. Dudzik, W. Kleemann, and H. Wende, Nat. Commun. **4**, 2051 (2013).

[49] A. Weiss, Ber. Bunsenges. Phys. Chem. **80**, 175 (1976).

[50] H. P. Rooksby and B. T. M. Willis, Nature (London) **172**, 1054 (1953).

[51] K. L. Lopez Maldonado, P. de la Presa, E. Flores Tavizón, R. Farias, J. A. Matutes-Aquino, A. Hernando Grande, and J. Elizalde Galindo, J. Appl. Phys. **113**, 17E132 (2013).

[52] P. Poddar, T. Fried, G. Markovich, A. Sharoni, D. Katz, T. Wizansky, and O. Millo, Europhys. Lett. **64**, 98 (2003).

[53] E. J. W. Verwey, Nature (London) **144**, 327 (1939).

[54] E. J. W. Verwey and P. W. Haayman, Physica (Amsterdam) **8**, 979 (1941).

[55] M. G. Chapline and S. X. Wang, J. Appl. Phys. **97**, 123901 (2005).

[56] A. Dediu, E. Arisi, I. Bergenti, A. Riminucci, M. Solzi, C. Pernechele, and M. Natali, J. Magn. Magn. Mater. **316**, e721 (2007).

[57] X. H. Liu, W. Liu, and Z. D. Zhang, Phys. Rev. B **96**, 094405 (2017).

[58] H.-T. Jeng, G. Y. Guo, and D. J. Huang, Phys. Rev. Lett. **93**, 156403 (2004).

[59] J. P. Wright, J. P. Attfield, and P. G. Radaelli, Phys. Rev. B **66**, 214422 (2002).

[60] M. Bohra and S. C. Sahoo, J. Alloys Compds. **699**, 1118 (2017).

[61] T. Dhakal, D. Mukherjee, R. Hyde, P. Mukherjee, M. H. Phan, H. Srikanth, and S. Witanachchi, J. Appl. Phys. **107**, 053914 (2010).

[62] S. E. Shirsath, X. Liu, Y. Yasukawa, S. Li, and A. Morisako, Sci. Rep. **6**, 30074 (2016).

[63] D. Mukherjee, M. Hordagoda, P. Lampen, M.-H. Phan, H. Srikanth, S. Witanachchi, and P. Mukherjee, J. Appl. Phys. **115**, 17D707 (2014).

[64] D. Mukherjee, T. Dhakal, M.-H. Phan, H. Srikanth, P. Mukherjee, and S. Witanachchi, Phys. B: Condens. Matter **406**, 2663 (2011).

[65] L. Shen, M. Althammer, N. Pachauri, B. Loukya, R. Datta, M. Iliev, N. Bao, and A. Gupta, J. Cryst. Growth **390**, 61 (2014).

[66] D. Mukherjee, N. Bingham, M.-H. Phan, H. Srikanth, P. Mukherjee, and A. S. Witanachchi, J. Appl. Phys. **111**, 07D730 (2012).

[67] See Supplemental Material at http://link.aps.org/supplemental/10.1103/PhysRevB.102.054433 for XRD rocking scans, XPS spectra of individual elements, temperature dependent XRD scans during heating, simulated crystal structure of CFO unit cell for CFO/LSMO/MgO heterostructure, temperature dependence of zero-field-cooled (ZFC) and field-cooled (FC) magnetisation for bulk CFO powder and CFO/LSMO/MgO heterostructure, Landau coefficients from measured isothermal magnetization data for CFO/LSMO/MgO, MC entropy change for CFO/LSMO/MgO up to 5 T magnetic field from field, and temperature dependent magnetization measurements.

[68] C. Himcinschi, I. Vrejoiu, G. Salvan, M. Fronk, A. Talkenberger, D. R. T. Zahn, D. Rafaja, and J. Kortus, J. Appl. Phys. **113**, 084101 (2013).

[69] M. De Santis, A. Bailly, I. Coates, S. Grenier, O. Heckmann, K. Hricovini, Y. Joly, V. Langlais, A. Y. Ramos, C. Richter, X. Torrelles, S. Garaudée, O. Geaymond, and O. Ulrich, Acta Cryst. B **75**, 8 (2019).

[70] T. Aghavnian, J. B. Moussy, D. Stanescu, R. Belkhou, N. Jedrecy, H. Magnan, P. Ohresser, M. A. Arrio, P. Sainctavit, and A. Barbier, J. Electron Spectrosc. Relat. Phenom. **202**, 16 (2015).

[71] F. He, B. O. Wells, Z. G. Ban, S. P. Alpay, S. Grenier, S. M. Shapiro, W. Si, A. Clark, and X. X. Xi, Phys. Rev. B **70**, 235405 (2004).

[72] J. Blasco, J. García, and G. Subías, Phys. Rev. B **83**, 104105 (2011).

[73] J.-p. Zhou, H.-c. He, and C.-W. Nan, Appl. Surf. Sci. **253**, 7456 (2007).

[74] V. V. Gridin, G. R. Hearne, and J. M. Honig, Phys. Rev. B **53**, 15518 (1996).

[75] D. Mukherjee, N. Bingham, M. Hordagoda, M.-H. Phan, H. Srikanth, S. Witanachchi, and P. Mukherjee, J. Appl. Phys. **112**, 083910 (2012).

[76] D. Mukherjee, M. Hordagoda, P. Lampen, M.-H. Phan, H. Srikanth, S. Witanachchi, and P. Mukherjee, Phys. Rev. B **91**, 054419 (2015).

[77] D. C. Jiles, J. Phys. D: Appl. Phys. **28**, 1537 (1995).

[78] D. Mukherjee, A. Datta, C. Kons, M. Hordagoda, S. Witanachchi, and P. Mukherjee, Appl. Phys. Lett. **105**, 212903 (2014).

[79] A. P. Roberts, Y. Cui, and K. L. Verosub, J. Geophys. Res.: Solid Earth **100**, 17909 (1995).

[80] J. Inoue and M. Shimizu, J. Phys. F: Metal Phys. **12**, 1811 (1982).

[81] P. E. Brommer, Phys. B: Condens. Matter **154**, 197 (1989).

[82] B. K. Banerjee, Phys. Lett. **12**, 16 (1964).

[83] P. Poddar, J. Gass, D. J. Rebar, S. Srinath, H. Srikanth, S. A. Morrison, and E. E. Carpenter, J. Magn. Magn. Mater. **307**, 227 (2006).
[84] E. V. Gopalan, I. A. Al-Omari, D. S. Kumar, Y. Yoshida, P. A. Joy, and M. R. Anantharaman, Appl. Phys. A **99**, 497 (2010).
[85] V. Franco and A. Conde, Int. J. Refrig. **33**, 465 (2010).
[86] V. Franco, A. Conde, J. M. Romero-Enrique, and J. S. Blázquez, J. Phys.: Condens. Matter **20**, 285207 (2008).
[87] V. Franco, J. S. Blázquez, and A. Conde, Appl. Phys. Lett. **89**, 222512 (2006).
[88] A. Arrott and J. E. Noakes, Phys. Rev. Lett. **19**, 786 (1967).
[89] T. D. Shen, R. B. Schwarz, J. Y. Coulter, and J. D. Thompson, J. Appl. Phys. **91**, 5240 (2002).
[90] Z. L. Liao, G. Koster, M. Huijben, and G. Rijnders, Sci. Rep. **7**, 2654 (2017).
[91] M. S. Anwar, F. Ahmed, and B. H. Koo, Acta Mater. **71**, 100 (2014).
[92] S. Akhter, D. P. Paul, S. M. Hoque, M. A. Hakim, M. Hudl, R. Mathieu, and P. Nordblad, J. Magn. Magn. Mater. **367**, 75 (2014).
[93] N. Chau, N. Thuan, D. Minh, and N. Luong, VNU J. Sci. Math.-Phys. **24**, 155 (2008).